Nuclear membrane protein Bqt4 maintains nuclear envelope integrity by recruiting phosphatidic acid

Yasuhiro Hirano[1,*], Tsukino Sato[2], Ayane Miura[2], Yoshino Kubota[1], Tomoko Shindo[3], Koichi Fukase[2], Tatsuo Fukagawa[1], Kazuya Kabayama[2], Tokuko Haraguchi[1] and Yasushi Hiraoka[1,*]

[1] Graduate School of Frontier Biosciences, Osaka University, Suita 565-0871, Japan

[2] Department of Chemistry, Graduate School of Science, Osaka University, Toyonaka, 560-0043, Japan

[3] School of Medicine, Keio University, Shinjuku-ku, Tokyo, 160-8582, Japan

[*] **Corresponding to:**

Yasuhiro Hirano (y.hirano.fbs@osaka-u.ac.jp) or Yasushi Hiraoka (hiraoka@fbs.osaka-u.ac.jp), Graduate School of Frontier Biosciences, Osaka University, 1-3 Yamadaoka, Suita 565-0871, Japan. Tel.: +81-6-6879-4621, FAX: +81-6-6789-4622

Abstract

The nuclear envelope (NE) is a permeable barrier that maintains nuclear–cytoplasmic compartmentalization and ensures nuclear function; however, it ruptures in various situations such as mechanical stress and mitosis. Although the protein components for sealing a ruptured NE have been identified, the mechanism by which lipid components are involved in this process remains to be elucidated. Here, we found that an inner nuclear membrane (INM) protein Bqt4 directly interacts with phosphatidic acid (PA) and serves as a platform for NE maintenance in the fission yeast *Schizosaccharomyces pombe*. The intrinsically disordered region (IDR) of Bqt4 proximal to the transmembrane domain binds to PA and forms a solid-phase aggregate *in vitro*. Excessive accumulation of Bqt4 IDR in INM results in membrane overproliferation and lipid droplet formation in the nucleus, leading to centromere dissociation from the NE and chromosome missegregation. Our findings suggest that Bqt4 IDR controls nuclear membrane homeostasis by recruiting PA to the INM, thereby maintaining the structural integrity of the NE.

36 **Introduction**

37 In eukaryotic cells, the nuclear envelope (NE) encapsulates chromosomes in the
38 nucleus. The NE functions as a permeable barrier to maintain nuclear–cytoplasmic
39 compartmentalization and ensures various nuclear functions. The NE comprises inner
40 and outer nuclear membranes (INM and ONM, respectively), which comprise lipid
41 membranes and transmembrane proteins. The INM interacts with chromosomes to
42 regulate their organization and genetic activity. The ONM is continuous with the
43 endoplasmic reticulum (ER). The integrity of the NE, which retains the nuclear barrier,
44 is crucial for cell viability (Webster and Lusk, 2016), and yet, the NE is dynamic and
45 undergoes repeated breakdown and reformation during mitosis (open mitosis) in higher
46 eukaryotic cells (Güttinger et al., 2009; Lajoie and Ullman, 2017; Ungricht and Kutay,
47 2017). The NE also ruptures occasionally because of nuclear damage, such as
48 mechanical stress, during the interphase (Denais et al., 2016). Thus, the ruptured NE
49 should be promptly resealed to ensure nuclear functions. Recent studies have identified
50 the components essential for NE sealing; however, the underlying mechanisms have not
51 been fully understood.

52 To reseal incidental NE ruptures, eukaryotic cells have a mechanism that
53 surveils and maintains the NE integrity. To maintain the NE integrity, the endosomal
54 sorting complex required for transport-III (ESCRT-III) is transiently recruited to the
55 rupture sites of the NE by charged multivesicular body protein 7 (CHMP7/Chm7/Cmp7
56 in metazoans, budding yeast *Saccharomyces cerevisiae*, and fission yeast
57 *Schizosaccharomyces pombe* and *japonicus*) (Gu et al., 2017; Olmos et al., 2015; Pieper
58 et al., 2020; Vietri et al., 2015; Von Appen et al., 2020). Lem2, a member of the
59 conserved LEM (Lap2β-Emerin-Man1) domain INM protein family, functions as a

60 nuclear adaptor for CHMP7 (Gu et al., 2017; Von Appen et al., 2020; Webster et al.,
61 2016). ESCRT-III seals membrane rupture sites during mitosis and interphase (Denais
62 et al., 2016; Raab et al., 2016). Recent studies have shown that this sealing mechanism
63 is highly conserved and plays a global role in diverse eukaryotes (Dey et al., 2020; Gu
64 et al., 2017).

65 In addition to the proteinaceous sealing executors, the NE rupture sealing
66 mechanism involves *de novo* lipid synthesis (Bahmanyar and Schlieker, 2020; Kinugasa
67 et al., 2019; Lee et al., 2020; Penfield et al., 2020). Glycerophospholipids are the major
68 components of cellular lipid membranes and their synthesis is required for nuclear
69 membrane expansion (Foo et al., 2023; Takemoto et al., 2016). Glycerophospholipid
70 synthesis in the NE is regulated by the phosphatidate phosphatase lipin (Ned1 in *S.*
71 *pombe*; Pah1 in *S. cerevisiae*), CNEP1 (an NE-localizing activator of lipin; Nem1-Spo7
72 complex in yeast), and phosphatidate cytidylyltransferase Dgk1 in metazoans (Han et
73 al., 2006; Romanauska and Köhler, 2018). In fungi, the cytidylyltransferase Cds1 (Bbl1
74 in *S. pombe*) catalyzes the conversion of phosphatidic acid (PA) to cytidine diphosphate
75 diacylglycerol (CDP-DAG), which is a major upstream reaction in phosphatidylcholine
76 (PC) and phosphatidylethanolamine (PE) synthesis (Carman and Han, 2009;
77 Siniossoglou, 2013). In *C. elegans* embryos, the CNEP1-lipin pathway has been
78 proposed to coordinate the production of ER membranes, which are utilized to narrow
79 the hole of NE ruptures (Bahmanyar, 2015; Bahmanyar et al., 2014; Penfield et al.,
80 2020) and ESCRT-III complexes restrict excess ER membrane supplements to the NE
81 holes (Penfield et al., 2020). These findings suggest that glycerophospholipid synthesis
82 is properly regulated during NE rupture sealing. Other lipid species and their properties
83 are also involved in sealing NE ruptures. The saturation level of fatty acyl chains differs

among different organelle membranes (Levental and Lyman, 2023). Recently, it has been reported that an imbalance of lipid saturation leads to NE rupture (Romanauska and Köhler, 2023) and overexpression of Δ9 fatty acid desaturase Ole1 in *S. japonicus* rescues NE sealing defects (Lee et al., 2020). Lipids containing long-chain fatty acids, such as ceramide, are involved in NE rupture sealing: overexpression of the very-long-chain fatty acid synthase Elo2 rescues the nuclear membrane rupture phenotype of Lem2 and Bqt4 double deletion mutant in *S. pombe* (Kinugasa et al., 2019). Moreover, accumulation of long-chain sphingoid bases suppresses NE morphology defects induced by aneuploidy (Hwang et al., 2019). Although the lipid components required for NE maintenance have been identified, how these lipids accumulate and function in the INM remains unclear.

Several hundred INM-specific proteins, such as LEM proteins and lamin B receptor, have been identified in mammalian cells (Korfali et al., 2012). INM proteins are involved in NE maintenance and potentially regulate nuclear membrane properties. In *S. pombe*, the INM proteins, Lem2 and Bqt4, play central roles in maintaining NE integrity. Loss of either Lem2 or Bqt4 does not affect cell viability, but loss of both confers a synthetic lethal phenotype accompanied by nuclear membrane rupture (Kinugasa et al., 2019; Tange et al., 2016), suggesting that these proteins share vital functions in NE rupture sealing. Lem2 is a multifunctional protein involved in many cellular processes such as gene expression and NE shaping (Banday et al., 2016; Barrales et al., 2016; Hirano et al., 2020; Kume et al., 2019; Martín Caballero et al., 2022; Tange et al., 2016). Among the wide range of Lem2 functions, the key function of Lem2 for NE maintenance is the recruitment of ESCRT-III to the NE (Gu et al., 2017; Lee et al., 2020; Pieper et al., 2020; Thaller et al., 2021; Von Appen et al., 2020). In

contrast to Lem2, the role of Bqt4 in NE maintenance has not been identified. Bqt4 was originally identified as a protein that anchors telomeres to the NE (Chikashige et al., 2009), but the telomere-anchoring function of Bqt4 is unnecessary for NE maintenance (Tange et al., 2016). Our recent studies have shown that excess Bqt4 accumulation in INM deforms the NE (Le et al., 2023) and Bqt4 interacts with Cwh43, an enzyme involved in triacylglycerol metabolism (Hirano et al., 2023a), suggesting that Bqt4 may regulate the properties of INM. Thus, in this study, we investigated the role of Bqt4 in NE maintenance and found that Bqt4 maintains NE integrity by recruiting PA-enriched membranes to the INM.

118 **Results**

119 **Vital Bqt4 domain required for cell growth**

120 To reveal a Bqt4 function in NE maintenance, we investigated functional domains of
121 Bqt4 using the *lem2*-shut-off *bqt4*Δ strain, which confers synthetic lethality upon shut-
122 off by the addition of thiamine (Hirano et al., 2023b; Kinugasa et al., 2019; Tange et al.,
123 2016). Bqt4 fragments were introduced into this strain and viability was tested under
124 shut-off conditions. We divided Bqt4 into three domains (schematic diagram in Fig. 1a):
125 1-140 amino acid (aa) residues containing APSES domain (named for Asm1p, Phd1p,
126 Sok2p, Efg1p, and StuAp), 141-262 aa residues containing a coiled-coil region, and
127 259-383 aa residues called a "homologous to apolipoprotein" region. GFP-tagged Bqt4
128 fragments deleted for each of these domains (Δ1-140, Δ141-262, and Δ259-383) were
129 expressed in the *lem2*-shut-off *bqt4*Δ cells and growth of the cells were observed. Upon
130 shut-off of *lem2*, the cells expressing Δ1-140 and Δ259-383 fragments of Bqt4 did not
131 grow, whereas the cells expressing Δ141-262 did (Fig. 1b). These results indicate that 1-
132 140 and 259-383 aa domains are essential for vital functions of Bqt4. All these
133 fragments as well as wild-type Bqt4 (FL) were localized to the NE (Fig. 1c), suggesting
134 that the lethality was not caused by the loss of NE localization.

135 The 259–383 aa region was annotated as "homologous to apolipoprotein."
136 Apolipoprotein is a co-factor protein that binds to lipoproteins, such as low-density
137 lipoprotein and high-density lipoprotein comprising cholesterol and triacylglyceride
138 particles covered with phospholipids, and mediates their transport and metabolism
139 (Mahley et al., 1984). Considering its properties, this region potentially binds to lipids
140 and is consequently involved in NE maintenance; however, this potential interaction has

141 not been experimentally demonstrated. Thus, in this study, we focused on the 259–383
142 aa region.
143
144 **KSE domain of Bqt4 is vital for NE maintenance**
145 To narrow down the vital domain in the 259-383 aa region, we predicted the secondary
146 structure of Bqt4 using the PSIPRED 4.0 prediction server
147 (http://bioinf.cs.ucl.ac.uk/psipred/; Supplementary Fig. 1a). From this prediction, we
148 examined the 340-383 aa region which consists of α-helix (340-363 aa) and low
149 complex regions (364-383 aa) (Fig. 1d and red and blue squared regions in
150 Supplementary Fig. 1a). The deletion mutants Δ340-383 and Δ364-383, but not Δ340-
151 363, showed growth defect in the *lem2*-shut-off *bqt4*Δ strain (Fig. 1e), indicating that
152 the 364-383 aa region possesses vital functions of Bqt4. The 364-383 aa region is biased
153 in positive charge, containing seven positive (K or R), six polar (S), and four negative
154 (E or D) amino acids out of the 20 amino acids (Supplementary Fig. 1a), hereafter
155 referred to as the KSE domain. The ΔKSE mutant as well as wild-type Bqt4 localized at
156 the NE (Fig. 1f) and retained interaction with Bqt3 (Supplementary Fig. 1b) and the
157 telomere anchoring (Supplementary Fig. 1c). Thus, this function is probably distinct
158 from the known Bqt4 functions.
159 We next examined whether the KSE domain is required for NE maintenance.
160 The ΔKSE mutant was expressed in *lem2*-shut-off *bqt4*Δ cells expressing GFP–GST–
161 NLS, a nuclear protein marker, and nuclear protein leakage from the nucleus was
162 assessed by calculating the fluorescence intensity ratio of nucleus to cytoplasm. Upon
163 thiamine addition, GFP–GST–NLS severely leaked from the nucleus of ΔKSE mutant-
164 expressing cells, but not from the nucleus of FL-expressing cells (Fig. 1g and h),

165 indicating NE rupture in the ΔKSE mutant-expressing cells. These results suggest that
166 the KSE domain is vital for NE maintenance.
167
168 **KSE-containing intrinsically disordered region (IDR) domain is responsible for**
169 **dominant-negative effect of Bqt4 overexpression**
170 We have previously reported that abnormal Bqt4 accumulation causes severe NE
171 deformation-associated growth defects (Le et al., 2023). As the KSE domain is involved
172 in NE maintenance, it may be responsible for this phenotype. To test this hypothesis,
173 GFP-tagged ΔKSE (Δ364-383 aa) or KSE (364-383 aa) protein was overexpressed in *S.*
174 *pombe* cells under the *nmt1* promotor. Overexpression of the ΔKSE fragment averted
175 the growth defects and NE deformation (Supplementary Fig. S2), suggesting that the
176 KSE region causes dominant-negative effects of Bqt4 overexpression; however, the
177 KSE region alone did not cause these defects (Supplementary Fig. S2), indicating that
178 the KSE region is essential, but not sufficient, for the dominant-negative effects of Bqt4
179 overexpression. A larger fragment containing the KSE region is necessary for the
180 dominant-negative effects.
181 Thus, we further searched for domains responsible for the growth defects
182 associated with severe NE deformation upon Bqt4 overexpression. For this purpose, we
183 examined the three-dimensional protein structure around the KSE domain predicted by
184 Alphafold2 (https://alphafold.ebi.ac.uk/entry/O60158) and selected an IDR (364-413 aa;
185 Fig. 2a) containing the KSE domain as a candidate. The IDR fragment of Bqt4 tagged
186 with GFP (GFP-IDR) was localized to the NE despite the absence of TM and
187 nucleoplasm under suppressive expression conditions (Fig. 2b, +thiamine). In contrast,
188 GFP-KSE was localized to nucleoplasm but not to the NE (Fig. 2c). When GFP-IDR

189 was overexpressed in *S. pombe* cells under the control of the *nmt1* promoter, its
190 overexpression resulted in severe growth defects in the spot assay (Fig. 2d). These
191 results indicate that the overexpression of IDR, but not KSE, confers dominant-negative
192 effects on cell growth and suggest that the IDR domain is substantial for NE
193 maintenance, causing loss-of-function and dominant-negative effects. We subsequently
194 focused on the IDR domain. The essentiality of the IDR domain for NE maintenance
195 could not be assessed because deleting the 384–413 aa region caused protein
196 degradation (Supplementary Fig. S3).
197
198 **Overexpression of IDR induces aberrant NE morphology**
199 Under overexpression conditions, GFP-IDR was localized in the nucleoplasm,
200 accompanied by a herniated structure adjacent to the nucleus (Fig. 2e, arrows). Ish1-
201 mCherry, a marker of NE, was faintly localized in the herniated region, suggesting that
202 the herniated region is somewhat atypical for NE. The Ish1 signal, which was localized
203 in the NE under normal conditions, was distributed on cytoplasmic membranes besides
204 the NE under overexpression conditions (Fig. 2e), suggesting that overexpression of
205 GFP-IDR may cause abnormal membrane proliferation. To confirm the direct effect of
206 IDR overexpression on the NE, we examined the GFP-IDR fragment with a
207 transmembrane domain (IDR-TM; 364-432 aa) and found that overexpression of GFP-
208 IDR-TM caused more severe defects than GFP-IDR in the NE structure, such as
209 herniation (Fig. 2f). These results suggest that the NE localization of overexpressed IDR
210 causes severe NE defects.
211 To further investigate the effects of IDR on NE structure, we observed cells
212 overexpressing IDR with correlative light-electron microscopy (CLEM) (Fig. 2g). We

213 found two major abnormalities: a vacuole-like structure covered with a multilayered
214 membrane within the nucleus, and electron-dense patches in the nucleoplasm (right
215 panel in Fig. 2g, red and blue arrows, respectively), both of which were not observed in
216 wild-type cells (Fig. 2h). The vacuole-like structure corresponded to the hole observed
217 in the fluorescence image (left panels in Fig. 2g, white arrows). In the herniated region,
218 where the IDR signal was concentrated, multilayered membranes extended to the
219 nuclear membrane, and these membranes surrounded the vacuoles. Such abnormal
220 vacuoles in the nucleus were located in close proximity to the NE, which is rich in
221 nuclear pore complexes (NPCs) (right panel in Fig. 2g, asterisks and Supplementary
222 Fig. 4 for serial sectioning images). Notably, the nuclear protein did not leak out of the
223 nucleus (Supplementary Fig. 5), indicating that the NE retained its function as a barrier
224 between the nucleus and the cytoplasm despite its abnormal morphology. The electron-
225 dense patches were distributed over a wide area within the nucleoplasm but were
226 scarcely distributed in the nucleolus (see serial sectioning images in Supplementary Fig.
227 4). Patches were observed in 45 of 50 nuclei overexpressing IDR. These results suggest
228 that the IDR domain of Bqt4 plays a role in maintaining the NE structure via its
229 membrane proliferation function.
230
231 **Overexpression of IDR induces aberrant chromosome organization**
232 The NE is an important architecture for chromosome organization in the nucleus.
233 Therefore, we investigated whether aberrant NE proliferation induced by Bqt4 affects
234 chromosome organization, in which centromeres form a cluster on the NE in *S. pombe*
235 cells. Overexpression of the GFP-IDR and GFP-IDR-TM fragments, but not GFP and
236 GFP-KSE, caused dissociation of the centromeres from the NE and their declustering

237 (Fig. 3a and b). This dissociation did not affect transcriptional silencing in the
238 centromeric region (Supplementary Fig. 6a). The Bqt4-binding protein, Lem2, which
239 binds to the central core of centromeres and is involved in centromere anchoring to the
240 NE, played a minor role in dissociation (Supplementary Fig. 6b and c). Time-lapse
241 observation of the cells overexpressing IDR-TM revealed that aberrant nuclear
242 membrane expansion occurred just after mitosis; subsequently, the clustered
243 centromeres started to dissociate from the NE and then declustered (Fig. 3c and
244 Supplementary Movie 1). Consequently, the chromosome was missegregated during the
245 next mitosis (Fig. 3c). Alternatively, the entire chromosome moved to one side or the
246 cells showed a *cut* phenotype (untimely torn cell phenotype); these cells displayed
247 nuclear membrane extrusion along the spindle microtubule (Supplementary Movie 2).
248 These phenotypes were similar to those of *ned1*-deficient cells; Ned1, a homolog of
249 human lipin, is a phosphatase that generates diacylglycerol (DAG) from PA, and the
250 *ned1-1 ts* mutant induces abnormal membrane proliferation (Tange et al., 2002). Taken
251 together, these observations suggest that NE overproliferation induced by IDR
252 accumulation causes genome instability.
253
254 **Bqt4 directly binds to PA via the IDR region**
255 The IDR region may be a potential lipid-binding domain because its accumulation in the
256 NE disrupts the membrane structure. To test this hypothesis, we performed a lipid
257 binding assay using a membrane lipid strip spotted on 15 different lipid types (Fig. 4a).
258 Purified His-GFP-tagged IDR fragments were incubated with the membrane, and bound
259 IDR fragments were detected. The IDR fragment was bound to PA and cardiolipin (Fig.
260 4a, IDR). In this study, we focused on PA in the following experiments because the

261 abnormal membrane proliferation observed with Bqt4 overexpression was similar to
262 that observed in the *ned1*-deficient phenotype. To confirm the binding of PA to the
263 IDR, we performed a liposome-mediated binding assay. Liposomes with different
264 percentages of PA were prepared and incubated with purified GFP-IDR protein. After
265 isolation of the liposomes via density gradient centrifugation, the proteins bound to the
266 liposomes were electrophoresed and detected using silver staining. GFP-IDR co-
267 sedimented with PA-containing liposomes but not with control liposomes (Fig. 4b).
268 Therefore, we conclude that the IDR region directly binds to PA *in vitro*.
269 Because PA and cardiolipin are negatively charged lipids (Fig. 4a), and the
270 IDR region, especially the KSE region, is biased toward a positive charge (Fig. 4c), we
271 assumed that the interaction between PA and the IDR region is mediated via
272 electrostatic interactions. To examine the contribution of these positive amino acids to
273 PA binding, we introduced mutations into the positive amino acids in the KSE region,
274 where four lysine and arginine residues were substituted with alanine (4KRA), and
275 expressed GFP-Bqt4-4KRA in the *lem2* shut-off stain. In addition, we substituted two
276 polar amino acid residues proximal to the positively charged portion with non-polar or
277 negative amino acids (2SA, 2SD, and 2SE) as controls. As predicted, the 4KRA mutant
278 did not restore lethality upon shut-off, whereas the other three mutants did (Fig. 4c),
279 supporting our hypothesis that the IDR and PA electrostatically interact with each other.
280 Next, we examined whether the lipid binding of Bqt4 affects its dynamics in INM using
281 fluorescence recovery after photobleaching (FRAP) (Fig. 4d). The FRAP analysis
282 revealed that GFP-ΔKSE and GFP-4KRA moved faster than full-length Bqt4 (GFP-FL)
283 in the INM, suggesting that Bqt4 forms a sub-stable complex with the INM by

284 interacting with PA. These results suggest that Bqt4 binds to PA via electrostatic
285 interactions in the IDR region and that this binding is crucial for Bqt4 function.
286
287 **IDR region forms solid-fibrous aggregate in the presence of PA**
288 Based on the predicted structural aspects of the IDR region, we assumed that this region
289 underwent phase separation in the presence of PA. To test this hypothesis, we
290 conducted an *in vitro* condensation assay. As protein concentration is an important
291 factor in analyzing phase separation, we determined the concentration of GFP-Bqt4 in
292 the NE using purified GFP as a standard; GFP-Bqt4 was integrated into the *lys1*$^{+}$ locus
293 and expressed under its own promoter. The protein concentration of Bqt4 in the NE
294 under authentic expression level was estimated to be approximately 1 μM
295 (Supplementary Fig. 7). In order to understand the phenomenon caused by the abnormal
296 accumulation of the IDR region, we used 2 μM, twice the normal amount, in further
297 experiments. Purified GFP-IDR protein was mixed with an increased concentration of
298 PA, and the mixture was observed using fluorescence microscopy. As shown in Fig. 5a
299 and b, GFP-IDR formed fibrous aggregates in a PA-dependent manner, indicating that
300 IDR can form aggregates. Consistent with the lipid binding assay results, aggregates
301 were not formed with the neutral phospholipid phosphatidylcholine (PC).
302 To further assess the aggregation state of GFP-IDR, we measured its molecular
303 dynamics using fluorescence correlation spectroscopy (FCS). Approximately 100 kHz
304 fluorescence intensity fluctuations accompanied by strong spike signals were observed
305 only for the GFP-IDR and PA mixture (Supplementary Fig. 8a). In addition, GFP-IDR
306 diffused slowly (Fig. 5c). In contrast, the fluctuations were less than 10 kHz for other
307 fragments (Supplementary Fig. 8a, compare inlets for GFP-IDR+PA and others). These

308 results indicate that IDR formed microscopically invisible as well as large visible
309 aggregates with PA.

310 Because the aggregates were not spherical, they were unlikely to be formed by
311 liquid-liquid phase separation (LLPS). To observe the molecular exchange rate in the
312 aggregates, we performed a FRAP assay. The molecular exchange rate was low in the
313 aggregates (Fig. 5d), supporting the idea that the aggregates are solid phase, not LLPS.
314 Collectively, the IDR tended to form a cluster in the presence of PA; subsequently, the
315 cluster transitioned into a large fibrous aggregate.

316 To explore the key properties of fibrous aggregate formation, we divided the
317 IDR into two fragments, GFP-tagged KSE (364-383 aa) and IDR-C (384-413 aa), and
318 evaluated their aggregation-forming activity in the presence of PA. GFP-KSE exhibited
319 marked aggregation-forming activity, whereas GFP-IDR-C showed much lower activity
320 than FL and KSE (Fig. 5e). As the positive charges in the KSE region restricted Bqt4
321 dynamics in the NE, as shown by the FRAP assay (Fig. 4d), the KSE region probably
322 restricts Bqt4 dynamics by forming solid-phase aggregates with PA. Nevertheless, IDR-
323 C should have a positive role in the membrane-association activity of IDR because the
324 activity of IDR was stronger than that of KSE (compare Fig. 2b and c).

325 To further test the functional differences between the KSE and IDR-C regions,
326 we incubated GFP-KSE and GFP-IDR-C in a molecular crowding solution containing
327 polyethyleneglycol (PEG) and assessed their ability to form aggregates. For this
328 experiment, we selected a protein concentration of 8 μM because of the following
329 reasons: 1) the ease of observation via a fluorescence microscope (Supplementary Fig.
330 8b) and 2) this concentration is in a range below the overexpression under the *nmt1*
331 promoter (Supplementary Fig. 7b). Contrary to the results of PA-mediated aggregate

332 formation (Fig. 5f), GFP-IDR-C exhibited aggregate formation similar to that of the
333 IDR region in the presence of PEG, whereas GFP-KSE did not (Fig. 5f). This result
334 suggests that the IDR-C region can facilitate aggregate formation once the KSE region
335 forms a cluster with PA and increases the local concentration of Bqt4 in the NE.
336 Finally, we tested the effect of additives on GFP-IDR aggregate formation
337 under crowding conditions to elucidate the dominant interaction type for aggregate
338 formation. NaCl, urea, arginine, 1,6-hexanediol (1,6-HD), sodium dodecyl sulfate
339 (SDS), and Triton X-100 (Tx-100) were used as salt, protein denaturant, protein
340 aggregation suppressor, aliphatic alcohol, ionic detergent, and non-ionic detergent,
341 respectively. Arginine and SDS drastically inhibited the aggregate formation among the
342 additives tested (Fig. 5g). These two additives also inhibited the aggregate formation of
343 the IDR-C fragment (Supplementary Fig. 9a). As arginine suppresses the hydrophobic
344 interactions of proteins by binding to the aromatic group, thus increasing the net charge
345 of the protein (Miyatake et al., 2016), the hydrophobic interaction between IDRs is
346 likely a dominant force in aggregation in *in vitro* condition. This result was consistent
347 with the finding that PA-induced aggregate formation because PA could strengthen the
348 hydrophobic interaction between the IDRs by neutralizing the positive charge in the
349 IDR, especially in the KSE region. These observations were consistent with the
350 molecular properties of the IDR region; the KSE and IDR-C regions were hydrophilic
351 and hydrophobic, respectively (Supplementary Fig. 9b and c). However, because the
352 aggregates were formed in the presence of NaCl, 1,6-HD, and Tx-100, multivalent
353 interactions might be involved in the aggregate formation of the IDRs. The IDR-derived
354 aggregates were soluble in low concentrations (0.1%) of SDS, suggesting that the
355 aggregates possess a similar property to fused in sarcoma (FUS) and hnRNPA2 (Kato et

356 al., 2012) and might be able to revert to a dispersion state in the cell, although they are
357 quite stable.
358 Taken together, these results demonstrate that the IDR region can form stable
359 aggregates with PA, which is accelerated by two distinct properties of the KSE and
360 IDR-C regions.
361
362 **Bqt4 is involved in regulating the balance of lipid synthesis by accumulating PA in**
363 **the INM**
364 Next, we investigated the biological significance of the interaction between IDR and
365 PA. Given our assumption that IDR overexpression changes the intracellular
366 localization of PA, we generated *S. pombe* cells expressing an mCherry-tagged PA
367 sensor that comprises a homodimer of the PA-binding helix of *S. cerevisiae* Opi1
368 bearing a G120W point mutation (Foo et al., 2023) to visualize PA localization. This
369 sensor was primarily localized in the nucleus and peripheral ER (Fig. 6a). In the cells
370 overexpressing FL, IDR-TM and IDR of Bqt4, intracellular localization of the PA
371 sensor was dramatically changed (Fig. 6a and b for quantification). In cells
372 overexpressing FL, the PA sensor accumulated in round structures beneath the NE that
373 were likely lipid droplets (LDs) covered with PA-containing phospholipids (Fig. 6a,
374 arrowheads in FL). These droplets were observed near the blebs of Bqt4 signals in the
375 NE. Similar PA accumulation in the nucleus was observed in IDR-TM–overexpressing
376 cells (IDR-TM in Fig. 6a and b for quantification). These results suggested that Bqt4
377 collects PA-enriched membranes to the NE via its IDR domain. In IDR-overexpressing
378 cells, GFP-IDR was localized in both the nucleoplasm and cytoplasm (Fig. 6a, IDR).
379 Consequently, the PA sensor was redistributed from the nucleus to the cytoplasm (Fig.

380 6a; IDR). In contrast, KSE overexpression did not alter the localization of the PA
381 sensor, although this fragment was localized in the cytoplasm, similar to IDR (Fig. 6a,
382 KSE). Therefore, we conclude that IDR, but not KSE, controls intracellular PA
383 localization depending on its localization and protein levels in *S. pombe* cells. As the
384 nuclear membrane over-proliferates following Bqt4 overexpression (Fig. 2), PA
385 recruitment possibly accelerates phospholipid synthesis in the NE.
386 As NE proteins are involved in regulating the balance between phospholipid
387 synthesis and energy storage by generating triacylglycerol (TAG) (Romanauska and
388 Köhler, 2018), our results indicate that Bqt4 accumulation forms LDs in the nucleus.
389 Thus, we examined the presence or absence of nuclear LDs in Bqt4-overexpressing
390 cells as a counterpart for phospholipid synthesis. As expected, the number of cells with
391 nuclear LDs increased in the cells overexpressing Bqt4-FL (Fig. 6c and d; 65.9%; see
392 arrowhead in FL) compared to the control cells under the suppressive conditions (0 –
393 0.3%). Overexpression of the IDR-TM and IDR region also led to an increased number
394 of cells with nuclear LDs (Fig. 6c and d; 62.9% and 28.6%, respectively). Most of the
395 nuclear LDs observed in the cells overexpressing IDR were localized in the herniated
396 NE (Fig. 6c; 75.8 ± 5.0%; arrowhead in IDR) that correspond to a vacuole-like structure
397 observed in the CLEM analysis (compare Fig. 3b with 6c). We also noticed that the LD
398 size in cells overexpressing FL, IDR-TM, and especially IDR, was larger than that in
399 cells under suppressive conditions (Fig. 6c and e). These results suggest that Bqt4
400 accumulation accelerates TAG synthesis in the NE. As both membrane
401 overproliferation and LD formation were accelerated, Bqt4 possibly plays a role in
402 orchestrating the balance of lipid synthesis via PA accumulation in the INM.

403 **Discussion**

404 In this study, we uncovered the non-telomeric vital function of Bqt4 in the context of
405 the synthetic lethal phenotype of *lem2*$^{+}$ and *bqt4*$^{+}$ double deletions. Bqt4 was initially
406 found to anchor telomeres to the NE via its association with the telomeric protein Rap1
407 (Chikashige et al., 2009). Bqt4 plays a vital role in the absence of Lem2 because the
408 double deletion of *bqt4*$^{+}$ and *lem2*$^{+}$ is lethal (Tange et al., 2016). However, the telomeric
409 function of Bqt4 is not vital, because double deletion of *rap1*$^{+}$ and *lem2*$^{+}$ is viable
410 (Tange et al., 2016). We found that Bqt4 plays a vital role in maintaining NE structures
411 by interacting with specific phospholipids such as PA. Excessive accumulation of Bqt4
412 on the NE caused membrane overproliferation and nuclear LD formation, which are
413 deleterious to cells (Figs. 2 and 6). Our previous reports showed that excess amounts of
414 Bqt4 are degraded via the ubiquitin-proteasome system, whereas Bqt4 bound to Bqt3 is
415 protected from degradation (Chikashige et al., 2009; Le et al., 2023). We speculate that
416 the protein level of Bqt4 is tightly regulated to maintain a functionally relevant lipid
417 composition in the INM.

418 The properties of Bqt4 identified in this study allow us to explain why NE
419 ruptures occur in cells lacking Lem2 and Bqt4, and how Bqt4 supports the repair of NE
420 ruptures. We propose that Bqt4 plays a role in NE maintenance via two distinct
421 pathways: (1) production of a preferable microenvironment at the NE rupture sites for
422 the robust association of the ESCRT-III complex, which is an executor of NE repair
423 (Olmos et al., 2015; Raab et al., 2016; Vietri et al., 2015), and (2) lipid supply via the
424 collection of the phospholipid precursor PA into the INM (Fig. 6f).

425 First, Bqt4 recruits Lem2 (Hirano et al., 2018) and PA (this study) to the NE,
426 playing an important role in functional ESCRT-III complex formation and consequently

427 producing a preferable microenvironment for repairing the ruptured NE membranes.
428 Cmp7/Chm7/CHMP7 accumulates at the rupture sites and recruits other ESCRT-III
429 components, such as Vps32 and Vps24. Lem2 acts as a nuclear adaptor to recruit Cmp7
430 to rupture sites (Gu et al., 2017; Von Appen et al., 2020). A recent study showed that
431 Chm7 directly binds to PA, and that this PA-binding ability is essential for the binding
432 of Chm7 to the NE (Thaller et al., 2021). As PA preferentially accumulates at the NE
433 holes, which have a high membrane curvature because of their small head group, the
434 ESCRT-III complex is efficiently formed at the NE holes. Moreover, Bqt4 interaction
435 with Lem2 and PA in *S. pombe* infers that Bqt4 recruits and accumulates them to the
436 NE rupture sites to assist Cmp7 in NE sealing, thus supporting the arrangement of
437 preferable membrane conditions for the ESCRT-III complex to seal NE ruptures.
438 Second, Bqt4 supplies lipids as membrane resources during NE sealing and
439 mitosis. As PA is a precursor of phospholipids, PA in INM produces major structural
440 membrane components, PC and PE; thus, the accumulation of PA by Bqt4 can
441 accelerate membrane expansion. Membrane overproliferation caused by Bqt4
442 accumulation was similar to that observed in Ned1/lipin and CTDNEP1/CENP-
443 1/Nem1-Spo7 mutants (Fig. 2 and Supplementary Movie 1) (Bahmanyar et al., 2014;
444 Penfield et al., 2020; Santos-Rosa et al., 2005; Tange et al., 2002), supporting this idea.
445 In fungi, PA is utilized for cytidine diphosphate diacylglycerol (CDP-DAG) synthesis
446 by cytidylyltransferase Cds1 (Bbl1 in *S. pombe*), which is a major upstream reaction in
447 PC and PE synthesis (Han et al., 2006). The Ned1 and Nem1-Spo7 complexes are
448 involved in the conversion of PA to DAG in the lipid storage pathway, which
449 antagonizes CDP-DAG synthesis in terms of PA utilization (reviewed in (Carman and
450 Han, 2009)). Loss-of-function mutations in either Ned1 or Nem1-Spo7 have been

451 reported to cause abnormal nuclear membrane expansion (Santos-Rosa et al., 2005;
452 Tange et al., 2002). In the present study, we observed membrane overproliferation (Fig.
453 2), PA accumulation (Fig. 6a), and LD formation in the nucleus (Fig. 6b) upon the
454 accumulation of Bqt4 in the NE. These results suggest that Bqt4 activates both
455 membrane expansion and lipid storage pathways by retaining PA in the INM that
456 diffuses from the ER. When the NE is ruptured, membrane resources are required to fill
457 the holes, and Bqt4 supports the phospholipid supply. In addition, as Bqt4 interacts with
458 enzymes involved in lipid metabolism in cooperation with Lem2 (Hirano et al., 2023a),
459 Bqt4 can also supply various membrane resources to NE holes. Considering that NE
460 sealing mechanisms can repair micron-scale holes larger than the ESCRT-III spiral
461 filament diameter (approximately 30-50 nm) (McCullough et al., 2015; Penfield et al.,
462 2020), Bqt4 likely supports the repair of NE holes of various sizes by mediating
463 membrane expansion.

464 Owing to the two Bqt4-mediated membrane repair processes discussed above,
465 the phase separation property of IDR with PA appears to be advantageous for collecting
466 the components necessary for NE sealing. We demonstrated that the electrostatic
467 interaction of the KSE region with PA enhanced stable aggregate formation via the
468 hydrophobic interaction of IDR-C *in vitro* (Fig. 5). This phenomenon is not an artificial
469 result of *in vitro* experiments but likely plays an important role in NE maintenance in *S.*
470 *pombe* cells because the 4KRA Bqt4 mutant loses its vital function and exhibits higher
471 dynamics than wild-type Bqt4 in the INM (Fig. 4c and d). The significance of molecular
472 clustering, including phase separation, of INM proteins for NE maintenance has also
473 been reported in other species: Lem2 undergoes phase separation via its low-complexity
474 domain, which is crucial for NE maintenance in human cells (Von Appen et al., 2020).

475 Considering this, the efficient collection of essential components via molecular
476 clustering of INM proteins appears to be a conserved mechanism for NE maintenance
477 across various organisms. Bqt4 was the first identified INM protein to regulate INM
478 properties by molecular clustering with lipids. Although Bqt4 is a *Schizosaccharomyces*
479 genus-specific protein, a similar membrane-bound protein bearing disordered regions
480 that interact with lipids may act as a functional homolog in other eukaryotes.

481 **Methods**

482 **Yeast strains and culture media**

483 All *S. pombe* and *S. cerevisiae* strains used in this study are listed in Supplementary
484 Table S1. Edinburgh minimal medium with glutamate (EMMG) or EMMG5S (EMMG
485 with 0.225 mg/mL adenine, leucine, uracil, lysine, and histidine) was used as the
486 minimum medium, and the rich medium was yeast extract with supplements (YES)
487 (Moreno et al., 1991). Cells were cultured in an appropriate medium at 30°C for 3-6
488 days, depending on their growth. Cell strains carrying *lem2*Δ were maintained in
489 EMMG to avoid genomic instability, which occurs in rich medium, as previously
490 reported (Hirano et al., 2018; Hirano et al., 2020; Kinugasa et al., 2019; Tange et al.,
491 2016). For selection, 100 µg/mL G418 disulfate (Nacalai Tesque, Kyoto, Japan), 200
492 µg/mL hygromycin B (FUJIFILM Wako Pure Chemical Corp., Osaka, Japan), 100
493 µg/mL nourseothricin sulfate (WERNER BioAgents, Jena, Germany), and 100 µg/mL
494 blastcidin S (FUJIFILM Wako Pure Chemical Corp.) were added to the media.

495

496 **Gene disruption, integration, and tagging**

497 Gene disruption, integration, and tagging were performed using a two-step PCR method
498 for direct chromosome integration as previously described (Bähler et al., 1998; Wach,
499 1996). Briefly, for the first-round PCR, ~500 bp genomic sequences upstream and
500 downstream of the open reading frames (ORFs) of interest were amplified through PCR
501 using KOD One (TOYOBO, Osaka, Japan; Cat. #KMM-201). These PCR products
502 were used as primers for the second round of PCR to amplify a template sequence
503 containing the selection markers. The resulting PCR products were transformed into *S.*
504 *pombe* cells for disruption, integration, and tagging, and transformants were selected on

505 an appropriate selection plate. The obtained strains were confirmed for correct
506 constructions of disruption, integration, and tagging via genomic PCR using KOD Fx
507 Neo (TOYOBO; Cat. #KFX-201) at both the 5′ and 3′ ends. In addition, we
508 performed genomic PCR on the ORF of the gene of interest to confirm the absence of
509 the ORF in the genome.
510
511 **Plasmid construction**
512 All plasmids used in this study were constructed using the NEBulider (New England
513 Biolabs, Ipswich, USA; Cat #E2621L) according to the manufacturer's protocol.
514 Restriction enzymes were purchased from TaKaRa Bio Inc. (Kusatsu, Japan) and New
515 England Biolabs (Ipswich, MA, USA). cDNA sequences encoding Bqt4 fragments were
516 amplified via PCR from the pCSS18 plasmid (Chikashige et al., 2009) and cloned into
517 the authentic *bqt4* promoter-harboring pCSS41 at *Bam*HI site. Deletion and point
518 mutants of Bqt4 were generated using inverse PCR. After confirming the DNA
519 sequences, these mutants were cloned into *nmt1* promoter harboring pCST3 at *Bam*HI
520 site or pGADT7-AD (Clontech) at *Eco*RI site. cDNA sequence of Bqt3 was amplified
521 and cloned into pGBKT7-DB (Clontech) at *Eco*RI and *Bam*HI sites for the yeast two-
522 hybrid assay. To express the Bqt4 protein in *E. coli*, cDNA sequences encoding GFP,
523 GFP-IDR (364-413 aa), GFP-KSE (364-383 aa), and GFP-IDR-C (384-413 aa) were
524 amplified via PCR and cloned into the pColdI vector (Clontech) at *Bam*HI site.
525 The DNA sequence of the PA biosensor *S. cerevisiae* (NLS) Opi1^{111-}
526 ^{189}2xAH^{G120w} (Foo et al., 2023), was synthesized using GenScript (Piscataway, NJ,
527 USA) and cloned into the pYK172 vector at *Bam*HI site.
528

529 **Spot assay**

530 *S. pombe* cells were cultured overnight in EMMG at 30°C to attain the logarithmic
531 growth phase. Five-fold serially diluted cells were spotted on EMMG plates
532 supplemented with or without 10 μM thiamine (initial cell numbers spotted are 4.0×10^3
533 cells) and cultured at 30°C for 3-4 days.

534

535 **Yeast two-hybrid assay**

536 The yeast two-hybrid assay was performed according to the manufacturer's protocol
537 (Clontech MATCHMAKER System Manual, Clontech). Plasmids harboring Bqt4 or
538 Bqt3 were co-transfected into *Saccharomyces cerevisiae* AH109 strain, and the cells
539 were grown on synthetic defined (SD) media with dropout supplements -Leu/-Trp (cat
540 #630417). To examine protein interactions, suspensions of the transformants (1.0×10^6
541 cells) were spotted onto SD plate media with dropout supplements, -Leu/-Trp or -Ade/-
542 His/-Leu/-Trp (cat #630428) (Takara Bio), and incubated at 30°C for 3 days.

543

544 **Protein expression and purification**

545 Plasmids harboring His-GFP, His-GFP-IDR, His-GFP-KSE, His-GFP-IDR-C were
546 introduced into the BL21 (DE3) pLysS strain. The cells were cultured in LB medium at
547 37 °C until OD_{600nm} ~0.5. After adding the final 0.1 mM Isopropyl β-D-1-
548 thiogalactopyranoside, the protein expression was induced at 16 °C for 24 h. The cells
549 were harvested, washed, and then resuspended in resuspension buffer (phosphate-
550 buffered saline [PBS] containing 0.1% Triton-X100 and 1 mM phenylmethylsulfonyl
551 fluoride). After sonication and centrifugation, the supernatant supplemented with final
552 10 mM imidazole was incubated with His-Select Nickel Affinity Gel (P6611, Lot No.

553 110M5166, SIGMA) for 1.5 h at 4 °C with rotation. The gel was washed three times
554 with resuspension buffer containing 10 mM imidazole, and the bound proteins were
555 eluted by stepwise treatment with 50, 100, and 300 mM imidazole. The purity and
556 quantity of the eluted proteins were assessed through SDS-PAGE followed by CBB
557 staining with BSA as a standard.
558
559 **Lipid binding assay**
560 Membrane lipid strip (P-6002) was purchased from Echelon Biosciences (Salt Lake
561 City, UT, USA). The membrane was incubated with blocking buffer (PBS containing
562 0.1% Triton X-100 and 3% fatty-acid- and globulin-free BSA [A7030, Lot No.
563 SLCH7959, SIGMA]) for 1 h at room temperature (approximately 26-28°C; RT), and
564 then incubated with 1 μM of His-GFP-IDR, or His-GFP in the blocking buffer for 1.5 h
565 at RT. After washing three times with washing buffer (PBS containing 0.1% Triton X-
566 100), the fluorescence emitted from bound proteins was detected by using ChemiDoc
567 Touch (Bio-Rad) equipped with a filter set for Alexa488.
568 For the liposome-binding assay, POPA (1-palmitoyl-2-oleoyl-*sn*-glycero-3-
569 phosphate; Cat. #840857C), POPC (1-oleoyl-2-palmitoyl-*sn*-glycero-3-phosphocholine;
570 Cat. #850475C) and POPE (1-palmitoyl-2-oleoyl-sn-glycero-3-phosphoethanolamine;
571 Cat. #850757C) in chloroform solution were purchased from Avanti Polar Lipids (NJ,
572 USA). Lipid solutions were mixed at specific ratios in round-bottomed glass tubes. The
573 solutions were blown dry under Argon gas in heating blocks at 45°C and resulting lipid
574 film was further dried under vacuum overnight. HEPES buffer (10 mM 4-(2-
575 hydroxyethyl)-1-piperazineethanesulfonic acid (HEPES)-NaOH (pH 7.6)) was added to
576 the tubes and hydrated with 10 mM liposome suspensions. The suspensions were

577 incubated in a 55°C water bath for 10 min and then shaken with a vortex mixer for 30 s.
578 This procedure was repeated three times. The freeze-thaw cycles were repeated at least
579 10 times between liquid nitrogen and a 55 °C water bath. The liposome solutions were
580 transferred to 5 × 41 mm ultracentrifuge tubes (Beckman Coulter, CA, USA; Cat.
581 #344090). Two millimolar liposomes were mixed with the indicated concentration of
582 proteins to a total volume of 150 µL. The mixed solutions were incubated at 30°C for 1
583 h, and then gently mixed an equal volume of 80% Histodentz (Sigma-Aldrich, MO,
584 USA; Cat. #D2158) in HEPES buffer and adjusted to 40% Histodenz. The mixture was
585 overlaid first with 250 µL of 30% Histodentz in HEPES buffer, then with 50 µL HEPES
586 buffer. Samples were spun at 200,000 × g at 4°C for 4 h in an MLS-50 rotor (Beckman
587 Coulter), and 60 µL of top layer was collected. After adding 18 µL of 4 × Laemmli
588 sample buffer and 2 µL of 2-mercaptoethanol to the collected fraction, samples were
589 denatured at 95°C for 5 min. Samples were electrophoresed in a 10% gel (Bio Craft,
590 Tokyo, Japan; Cat. #SDG-521) and visualized using 2D-Silver Stain Reagent II (Cosmo
591 Bio, Tokyo, Japan; Cat. #423413).
592
593 **Determination of Bqt4 concentration in the NE**
594 Cells expressing GFP-Bqt4 under the *bqt4* or *nmt1* promoter were attached to a glass-
595 bottom dish (MatTek, Cat #P35G-1.5-14-C) coated with soybean lectin (Sigma-Aldrich,
596 St. Louis, USA; Cat #L1395). Serially diluted purified His-GFP was dropped onto the
597 cells, and then the cells and GFP were simultaneously observed through spinning disk
598 confocal microscopy as described in "Microscopic observation." The fluorescence
599 intensities outside the cells were quantified, plotted, and used as a standard to quantify
600 the Bqt4 concentration.

601

602 **In vitro condensation assay**

603 For condensation assay with PA, the purified GFP, GFP-IDR, GFP-KSE, and GFP-
604 IDR-C proteins (final 2 μM) were mixed with 0, 20, 50, 100 nmol PA or PC on ice, and
605 2 μL of the mixture was put onto a cover glass (No. 1-S, Matsunami, Osaka, Japan)
606 immediately. For condensation assay in crowding condition, the GFP-Bqt4 fragments
607 (final 2 or 8 μM) were diluted into crowding buffer (25 mM Tris-HCl pH 7.5, 5 mM
608 $MgCl_2$, 1 mM dithiothreitol, 5% glycerol) with or without 5% PEG8000. Final 0.5 M
609 NaCl, 2 M urea, 0.2 M arginine, 10% 1,6-HD, 0.1% SDS, and 0.1% triton-X100 were
610 added to condensation buffer with PEG8000 to prevent aggregate formation. The
611 formed aggregates were observed through spinning disk confocal microscopy as
612 described in "Microscopic observation."

613

614 **Microscopic observation**

615 *S. pombe* cells were observed using a DeltaVision Elite system (GE Healthcare Inc.,
616 Chicago, USA) equipped with a pco.edge 4.2 sCMOS (PCO, Kelheim, Germany) and a
617 60× PlanApo N OSC oil-immersion objective lens (numerical aperture [NA] = 1.4,
618 Olympus, Tokyo, Japan). Intracellular localization of GFP-S65T (designated "GFP"
619 throughout this study) and mCherry fusion proteins was observed in living cells. For
620 time-lapse imaging, cells were cultured overnight in EMMG medium at 30°C to attain
621 the logarithmic growth phase before being placed in a glass-bottom culture dish. The
622 cells were attached to the glass via soybean lectin and covered with EMMG medium.

623 For the condensation assay and quantification of the GFP-Bqt4 concentration in
624 NE, a spinning disk confocal microscope system (CSU-W1; YOKOGAWA, Kanazawa,

625 Japan) equipped with an Orca-Fusion BT sCMOS camera (HAMAMATSU Photonics,
626 Hamamatsu, Japan) and a 60× PlanApo VC oil-immersion objective lens (numerical
627 aperture [NA] = 1.4; Nikon, Tokyo, Japan) was used. The microscope was operated
628 using the built-in NIS-Elements software (v5.42.01).
629 Chromatic aberration, except for time-lapse observations for multicolor images,
630 was corrected using Chromagnon software (v0.90) with a four-color fluorescence bead
631 (Thermo Fisher Scientific) image as a reference (Matsuda et al., 2018). Optical section
632 images captured by the DeltaVision Elite system were presented after deconvolution
633 using the built-in SoftWoRx software (v7.0.0). The brightness of the images was
634 changed using Fiji (Schindelin et al., 2012) or Adobe Photoshop 2022 software for
635 better visualization and presentation without changing the gamma settings.
636 FRAP analysis was performed as described previously with slight modifications
637 (Hirano et al., 2018). *S. pombe* cells were attached to a CELLVIEW cell culture dish
638 (Griner Bio-one, Austria; Cat. #627871) coated with soybean lectin. The mobility of
639 wild-type Bqt4 and its mutants was analyzed using an LSM780 confocal microscope
640 system (Carl Zeiss, Jena, Germany) equipped with a 63× oil-immersion objective lens
641 (NA = 1.4). For the FRAP analysis in cells, three images were collected before
642 bleaching (approximately 1% transmission of a 488-nm argon laser, 970 ms/frame, 1.58
643 μs/pixel, average 2, 512 × 256 pixels, 48 μm pinhole corresponding to 1 airy unit, 7×
644 zoom); the NE signal was bleached using 100% of a 488-nm laser with three iterations,
645 followed by the capture of a further 47 images, using the original setting. For FRAP
646 assay of GFP-IDR aggregate, the following condition was used: a 40× C-Apochromat
647 water-immersion objective lens (NA = 1.2) was used. Five images were collected before
648 bleaching (approximately 0.02% transmission of a 488-nm argon laser, 968 ms/frame,

649 3.15 μs/pixel, average 1, 512 × 256 pixels, 33.8 μm pinhole corresponding to 1 airy
650 unit, 4× zoom); the part of the aggregate was bleached using 100% of a 488-nm laser
651 with three iterations, followed by the capture of a further 95 images, using the original
652 setting. The fluorescence intensity in the bleached region was quantified using Zen 2.3
653 SP1 software. Photobleaching during imaging was monitored and normalized before the
654 recovery curve was plotted. The curve was plotted as a relative value and the average
655 fluorescence intensity before bleaching was 1.
656 FCS measurements were performed using an LSM510META confocor2 (Carl
657 Zeiss) equipped with a 40× C-apochromatic water immersion objective lens. The
658 measurements were performed using the built-in AIM software (version 3.2 SP2). GFP
659 proteins were excited using argon laser (488 nm) and the fluorescence passed a pinhole
660 (70 μm in diameter). The band-pass filter (530-600 nm) was detected using an
661 avalanche photodiode. The fluctuation in fluorescence intensity was measured for 10 s
662 in 10 cycles. The averaged autocorrelation function curves are presented.
663
664 **CLEM imaging**
665 CLEM imaging was performed as described previously (Asakawa et al., 2014; Asakawa
666 et al., 2016). Briefly, cells expressing Bqt4 fragments were cultured overnight in
667 EMMG to express Bqt4 proteins. The cells were attached to a dish with a gridded
668 coverslip (Ibidi, Martinsried, Germany) as described above and fixed by replacing the
669 medium with a fixative (4% paraformaldehyde, 250 mM Hepes-NaOH, pH 7.2) for 10
670 min at RT. During fixation, the cells were observed via fluorescence microscopy
671 (DeltaVision system), and then further fixed overnight with fresh fixative (2%
672 glutaraldehyde in 0.1 M sodium phosphate buffer, pH 7.2) at 4°C. After washing with

673 phosphate buffer, the cells were post-fixed in 1.2% $KMnO_4$ overnight, dehydrated, and
674 embedded in epoxy resin. Serial sections of 80 nm thickness were stained with uranyl
675 acetate and lead citrate and analyzed using a transmission electron microscope
676 (JEM1400Plus, JEOL, Japan) at 100 kV.
677
678 **Western blotting**
679 Cells cultured in the appropriate minimum medium, as described above, were harvested
680 at the mid-log phase using centrifugation. The cells were lysed in 1.85 N NaOH for 15
681 min on ice. Proteins were precipitated by adding 27.5% trichloroacetic acid. After
682 washing the precipitated proteins twice with ice-cold acetone, they were resolved in 2×
683 Laemmli SDS sample buffer without dye. The protein concentration was quantified
684 using a bicinchoninic acid assay (Thermo Fisher Scientific, Waltham, MA, USA; cat.
685 #23225) according to the manufacturer's protocol. The same amount of total protein (10
686 μg) was subjected to SDS-PAGE and then transferred to a polyvinylidene fluoride
687 membrane. The fluorescent proteins were probed with anti-GFP monoclonal (JL8,
688 1:2,000 dilution; TaKaRa Bio Inc.) and anti-RFP polyclonal (PM005, 1:5,000 dilution;
689 MBL, Nagoya, Japan) antibodies, and detected using chemiluminescence (ImmunoStar
690 LD, FUJIFILM Wako Pure Chemical Corp.). The membrane was stained with Amido
691 black to determine the amount of loaded proteins.
692
693 **Quantification, statistics, and reproducibility**
694 For phenotypic quantification of NE deformation, images were collected from at least
695 three independent experiments. Percentages of the phenotype were calculated in each
696 experiment (total number of cells examined was> 500), and the values are represented

697 as mean with standard deviation. LD size was measured using default functions in the
698 Fiji software. The fluorescence intensity line profile of each LDs was measured and
699 fitted as a Gaussian, and the full-width at half-maximum of the LD was calculated from
700 the fitted parameter. The values obtained from 100 LDs were plotted as violin plots.
701 Significance was assessed using the chi-square test, Tukey's test, or unpaired two-tailed
702 Student's *t*-test, as noted in the figure legends, using GraphPad Prism 9.4.1 or later
703 version.
704
705 **Data availability**
706 The data supporting the findings of this study are available in the paper and
707 Supplementary Information files. Additional data sets are available from the
708 corresponding author upon request.
709

Acknowledgments

We thank Chizuru Ohtsuki for her technical assistance. This study was supported by JSPS KAKENHI Grant Numbers JP19K06489 and JP20H05891 (to Y. Hirano); JP18K05356 (to K.K.); JP18H05528 (to T.H.), and JP18H05533, JP19K22389, and JP20H00454 (to Y. Hiraoka), and also by the grant of CREST of JST (JPMJCR21E6) to TF.

Author Contributions

Y. Hirano, TS, AM, KK, TF, TH and Y. Hiraoka conceived and designed the experiments. Y. Hirano, TS, AM, YK, TS and KK performed experiments and analyzed the data. Y. Hirano generated figures with the input from TS, AM, YK, TS, TH and Y. Hiraoka. KF supervised TS, AM with KK. Y. Hirano, TH and Y. Hiraoka wrote the manuscript with input from all the co-authors.

Declaration of Interests

The authors declare no competing financial or non-financial interests.

Contact for reagent and resource sharing

Further information and requests for resources and reagents should be directed to Yasuhiro Hirano (y.hirano.fbs@osaka-u.ac.jp) or Yasushi Hiraoka (hiraoka@fbs.osaka-u.ac.jp)

References

Asakawa, H., Hirano, Y., Shindo, T., Haraguchi, T. and Hiraoka, Y. (2022). Fission yeast Ish1 and Les1 interact with each other in the lumen of the nuclear envelope. *Genes Cells* **27**,643-656.

Asakawa, H., Hiraoka, Y. and Haraguchi, T. (2014). A method of correlative light and electron microscopy for yeast cells. *Micron* **61**, 53-61.

Asakawa, H., Yang, H. J., Hiraoka, Y. and Haraguchi, T. (2016). Virtual Nuclear Envelope Breakdown and Its Regulators in Fission Yeast Meiosis. *Front Cell Dev Biol* **4**, 5.

Bahmanyar, S. (2015). Spatial regulation of phospholipid synthesis within the nuclear envelope domain of the endoplasmic reticulum. *Nucleus* **6**, 102-106.

Bahmanyar, S., Biggs, R., Schuh, A. L., Desai, A., Müller-Reichert, T., Audhya, A., Dixon, J. E. and Oegema, K. (2014). Spatial control of phospholipid flux restricts endoplasmic reticulum sheet formation to allow nuclear envelope breakdown. *Genes & Dev.* **28**, 121-126.

Bahmanyar, S. and Schlieker, C. (2020). Lipid and protein dynamics that shape nuclear envelope identity. *Mol. Biol. Cell* **31**, 1315-1323.

Banday, S., Farooq, Z., Rashid, R., Abdullah, E. and Altaf, M. (2016). Role of Inner Nuclear Membrane Protein Complex Lem2-Nur1 in Heterochromatic Gene Silencing. *J. Biol. Chem.* **291**, 20021-20029.

Barrales, R. R., Forn, M., Georgescu, P. R., Sarkadi, Z. and Braun, S. (2016). Control of heterochromatin localization and silencing by the nuclear membrane protein Lem2. *Genes Dev.* **30**, 133-148.

Bähler, J., Wu, J. Q., Longtine, M. S., Shah, N. G., McKenzie, A., Steever, A. B., Wach, A., Philippsen, P. and Pringle, J. R. (1998). Heterologous modules for efficient and versatile PCR-based gene targeting in *Schizosaccharomyces pombe*. *Yeast* **14**, 943-51.

Carman, G. M. and Han, G. S. (2009). Phosphatidic Acid Phosphatase, a Key Enzyme in the Regulation of Lipid Synthesis. *J. Biol. Chem.* **284**, 2593-2597.

Chen, F. J., Yin, Y., Chua, B. T. and Li, P. (2020). CIDE family proteins control lipid homeostasis and the development of metabolic diseases. *Traffic* **21**, 94-105.

Chikashige, Y., Yamane, M., Okamasa, K., Tsutsumi, C., Kojidani, T., Sato, M., Haraguchi, T. and Hiraoka, Y. (2009). Membrane proteins Bqt3 and -4 anchor telomeres to the nuclear envelope to ensure chromosomal bouquet formation. *J. Cell Biol.* **187**, 413-427.

Denais, C. M., Gilbert, R. M., Isermann, P., Mcgregor, A. L., Te Lindert, M., Weigelin, B., Davidson, P. M., Friedl, P., Wolf, K. and Lammerding, J. (2016). Nuclear envelope rupture and repair during cancer cell migration. *Science* **352**, 353-358.

Dey, G., Culley, S., Curran, S., Schmidt, U., Henriques, R., Kukulski, W. and Baum, B. (2020). Closed mitosis requires local disassembly of the nuclear envelope. *Nature* **585**, 119-123.

Foo, S., Cazenave-Gassiot, A., Wenk, M. R. and Oliferenko, S. (2023). Diacylglycerol at the inner nuclear membrane fuels nuclear envelope expansion in closed mitosis. *J. Cell Sci.* **136**, jcs260568.

Gu, M., LaJoie, D., Chen, O. S., von Appen, A., Ladinsky, M. S., Redd, M. J., Nikolova, L., Bjorkman, P. J., Sundquist, W. I., Ullman, K. S. et al. (2017). LEM2 recruits CHMP7 for ESCRT-mediated nuclear envelope closure in fission yeast and

human cells. *Proc. Natl. Acad. Sci. U S A* **114**, E2166-E2175.
Güttinger, S., Laurell, E. and Kutay, U. (2009). Orchestrating nuclear envelope disassembly and reassembly during mitosis. *Nat. Rev. Mol. Cell Biol.* **10**, 178-191.
Han, G.-S., Wu, W.-I. and Carman, G. M. (2006). The *Saccharomyces cerevisiae* Lipin Homolog Is a Mg^{2+}-dependent Phosphatidate Phosphatase Enzyme. *J. Biol. Chem.* **281**, 9210-9218.
Hirano, Y., Kinugasa, Y., Asakawa, H., Chikashige, Y., Obuse, C., Haraguchi, T. and Hiraoka, Y. (2018). Lem2 is retained at the nuclear envelope through its interaction with Bqt4 in fission yeast. *Genes Cells* **23**, 122-135.
Hirano, Y., Kinugasa, Y., Kubota, Y., Obuse, C., Haraguchi, T. and Hiraoka, Y. (2023a). Inner nuclear membrane proteins Lem2 and Bqt4 interact with different lipid synthesis enzymes in fission yeast. *J. Biochem*. **30**, 33-46
Hirano, Y., Kinugasa, Y., Osakada, H., Shindo, T., Kubota, Y., Shibata, S., Haraguchi, T. and Hiraoka, Y. (2020). Lem2 and Lnp1 maintain the membrane boundary between the nuclear envelope and endoplasmic reticulum. *Commun. Biol.* **3,** 276.
Hirano, Y., Ohno, Y., Kubota, Y., Fukagawa, T., Kihara, A., Haraguchi, T. and Hiraoka, Y. (2023b). Ceramide synthase homolog Tlc4 maintains nuclear envelope integrity via its Golgi translocation. *J. Cell Sci.* **136**, jcs260923.
Structure **27**, 335-343.e3.
Hwang, S., Williams, J. F., Kneissig, M., Lioudyno, M., Rivera, I., Helguera, P., Busciglio, J., Storchova, Z., King, M. C. and Torres, E. M. (2019). Suppressing Aneuploidy-Associated Phenotypes Improves the Fitness of Trisomy 21 Cells. *Cell Rep.* **29**, 2473-2488.e5.
Kato, M., Han, T. W., Xie, S., Shi, K., Du, X., Wu, L. C., Mirzaei, H., Goldsmith, E. J., Longgood, J., Pei, J. et al. (2012). Cell-free formation of RNA granules: low complexity sequence domains form dynamic fibers within hydrogels. *Cell* **149**, 753-67.
Kinugasa, Y., Hirano, Y., Sawai, M., Ohno, Y., Shindo, T., Asakawa, H., Chikashige, Y., Shibata, S., Kihara, A., Haraguchi, T. et al. (2019). Very-long-chain fatty acid elongase Elo2 rescues lethal defects associated with loss of the nuclear barrier function. *J. Cell Sci.* **132**, jcs229021.
Korfali, N., Wilkie, G. S., Swanson, S. K., Srsen, V., De Las Heras, J., Batrakou, D. G., Malik, P., Zuleger, N., Kerr, A. R. W., Florens, L. et al. (2012). The nuclear envelope proteome differs notably between tissues. *Nucleus* **3**, 552-564
Kume, K., Cantwell, H., Burrell, A. and Nurse, P. (2019). Nuclear membrane protein Lem2 regulates nuclear size through membrane flow. *Nat. Commun.* **10,** 1871.
Lajoie, D. and Ullman, K. S. (2017). Coordinated events of nuclear assembly. *Cur. Opin. Cell Biol.* **46**, 39-45.
Le, T. K., Hirano, Y., Asakawa, H., Okamoto, K., Fukagawa, T., Haraguchi, T. and Hiraoka, Y. (2023). A ubiquitin-proteasome pathway degrades the inner nuclear membrane protein Bqt4 to maintain nuclear membrane homeostasis. *J. Cell Sci.* **136**, jcs260930
Lee, I. J., Stokasimov, E., Dempsey, N., Varberg, J. M., Jacob, E., Jaspersen, S. L. and Pellman, D. (2020). Factors promoting nuclear envelope assembly independent of the canonical ESCRT pathway. *J. Cell Biol.* **219**, e201908232
Levental, I. and Lyman, E. (2023). Regulation of membrane protein structure and function by their lipid nano-environment. *Nat. Rev. Mol. Cell Biol.* **24**, 107-122.
Lujan, P. and Campelo, F. (2021). Should I stay or should I go? Golgi membrane

spatial organization for protein sorting and retention. *Arch. Biochem. Biophys.* **707**, 108921.

Martín Caballero, L., Capella, M., Barrales, R. R., Dobrev, N., Van Emden, T., Hirano, Y., Suma Sreechakram, V. N., Fischer-Burkart, S., Kinugasa, Y., Nevers, A. et al. (2022). The inner nuclear membrane protein Lem2 coordinates RNA degradation at the nuclear periphery. *Nat. Struct. Mol. Biol.* **29**, 910-921.

Matsuda, A., Schermelleh, L., Hirano, Y., Haraguchi, T. and Hiraoka, Y. (2018). Accurate and fiducial-marker-free correction for three-dimensional chromatic shift in biological fluorescence microscopy. *Sci. Rep.* **8**, 7583.

McCullough, J., Clippinger, A. K., Talledge, N., Skowyra, M. L., Saunders, M. G., Naismith, T. V., Colf, L. A., Afonine, P., Arthur, C., Sundquist, W. I. et al. (2015). Structure and membrane remodeling activity of ESCRT-III helical polymers. *Science* **350**, 1548-51.

Miyatake, T., Yoshizawa, S., Arakawa, T. and Shiraki, K. (2016). Charge state of arginine as an additive on heat-induced protein aggregation. *Int. J. Biol. Macromol.* **87**, 563-9.

Moreno, S., Klar, A. and Nurse, P. (1991). Molecular genetic analysis of fission yeast *Schizosaccharomyces pombe*. *Methods Enzymol.* **194**, 795-823.

Olmos, Y., Hodgson, L., Mantell, J., Verkade, P. and Carlton, J. G. (2015). ESCRT-III controls nuclear envelope reformation. *Nature* **522**, 236-239.

Penfield, L., Shankar, R., Szentgyörgyi, E., Laffitte, A., Mauro, M. S., Audhya, A., Müller-Reichert, T. and Bahmanyar, S. (2020). Regulated lipid synthesis and LEM2/CHMP7 jointly control nuclear envelope closure. *J. Cell Biol.* **219**, e201908179.

Pieper, G. H., Sprenger, S., Teis, D. and Oliferenko, S. (2020). ESCRT-III/Vps4 Controls Heterochromatin-Nuclear Envelope Attachments. *Dev. Cell* **53**, 27-41.e6.

Raab, M., Gentili, M., de Belly, H., Thiam, H. R., Vargas, P., Jimenez, A. J., Lautenschlaeger, F., Voituriez, R., Lennon-Duménil, A. M., Manel, N. et al. (2016). ESCRT III repairs nuclear envelope ruptures during cell migration to limit DNA damage and cell death. *Science* **352**, 359-62.

Romanauska, A. and Köhler, A. (2018). The Inner Nuclear Membrane Is a Metabolically Active Territory that Generates Nuclear Lipid Droplets. *Cell* **174**, 700-715.e18.

Romanauska, A. and Köhler, A. (2023). Lipid saturation controls nuclear envelope function. *Nat. Cell Biol*. **25**, 1290-1302.

Santos-Rosa, H., Leung, J., Grimsey, N., Peak-Chew, S. and Siniossoglou, S. (2005). The yeast lipin Smp2 couples phospholipid biosynthesis to nuclear membrane growth. *EMBO J.* **24**, 1931-1941.

Schindelin, J., Arganda-Carreras, I., Frise, E., Kaynig, V., Longair, M., Pietzsch, T., Preibisch, S., Rueden, C., Saalfeld, S., Schmid, B. et al. (2012). Fiji: an open-source platform for biological-image analysis. *Nat. Methods* **9**, 676-682.

Siniossoglou, S. (2013). Phospholipid metabolism and nuclear function: roles of the lipin family of phosphatidic acid phosphatases. *Biochim. Biophys. Acta* **1831**, 575-81.

Takemoto, A., Kawashima, S. A., Li, J. J., Jeffery, L., Yamatsugu, K., Elemento, O. and Nurse, P. (2016). Nuclear envelope expansion is crucial for proper chromosomal segregation during a closed mitosis. *J. Cell Sci.* **129**, 1250-9.

Tange, Y., Chikashige, Y., Takahata, S., Kawakami, K., Higashi, M., Mori, C., Kojidani, T., Hirano, Y., Asakawa, H., Murakami, Y. et al. (2016). Inner nuclear membrane protein Lem2 augments heterochromatin formation in response to nutritional

875 conditions. *Genes Cells* **21**, 812-832.
876 **Tange, Y., Hirata, A. and Niwa, O.** (2002). An evolutionarily conserved fission yeast
877 protein, Ned1, implicated in normal nuclear morphology and chromosome stability,
878 interacts with Dis3, Pim1/RCC1 and an essential nucleoporin. *J. Cell Sci.* **115**, 4375-
879 4385.
880 **Thaller, D. J., Tong, D., Marklew, C. J., Ader, N. R., Mannino, P. J., Borah, S.,**
881 **King, M. C., Ciani, B. and Lusk, C. P.** (2021). Direct binding of ESCRT protein Chm7
882 to phosphatidic acid–rich membranes at nuclear envelope herniations. *J. Cell Biol.* **220**,
883 e202004222.
884 **Ungricht, R. and Kutay, U.** (2017). Mechanisms and functions of nuclear envelope
885 remodelling. *Nat. Rev. Mol. Cell Biol.* **18**, 229-245.
886 **Vietri, M., Schink, K. O., Campsteijn, C., Wegner, C. S., Schultz, S. W., Christ, L.,**
887 **Thoresen, S. B., Brech, A., Raiborg, C. and Stenmark, H.** (2015). Spastin and
888 ESCRT-III coordinate mitotic spindle disassembly and nuclear envelope sealing. *Nature*
889 **522**, 231-235.
890 **Von Appen, A., Lajoie, D., Johnson, I. E., Trnka, M. J., Pick, S. M., Burlingame, A.**
891 **L., Ullman, K. S. and Frost, A.** (2020). LEM2 phase separation promotes ESCRT-
892 mediated nuclear envelope reformation. *Nature* **582**, 115-118.
893 **Wach, A.** (1996). PCR-synthesis of marker cassettes with long flanking homology
894 regions for gene disruptions in *S. cerevisiae*. *Yeast* **12**, 259-65.
895 **Webster, B. M. and Lusk, C. P.** (2016). Border Safety: Quality Control at the Nuclear
896 Envelope. *Trends Cell Biol.* **26**, 29-39.
897 **Webster, B. M., Thaller, D. J., Jäger, J., Ochmann, S. E., Borah, S. and Lusk, C. P.**
898 (2016). Chm7 and Heh1 collaborate to link nuclear pore complex quality control with
899 nuclear envelope sealing. *EMBO J.* **35**, 2447-2467.
900

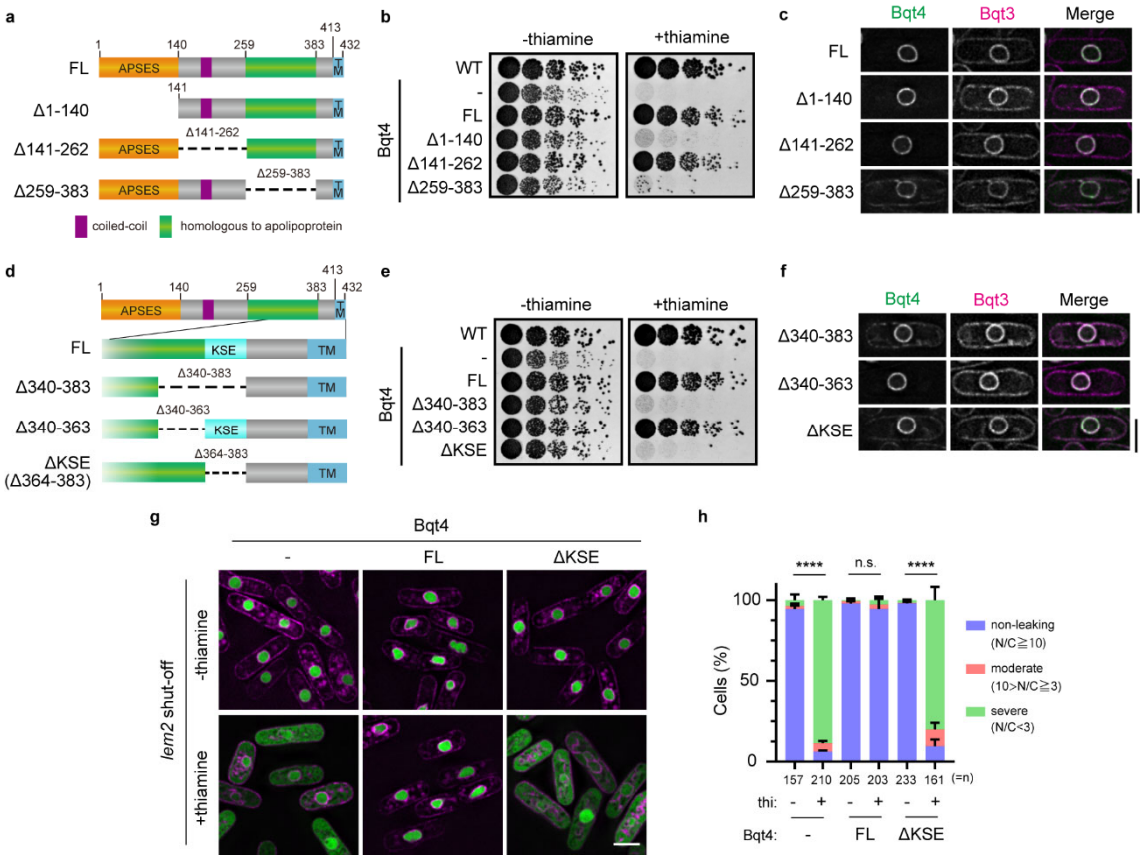

Figure 1. Vital domains for Bqt4 function

a. Schematic diagrams of the Bqt4-deletion mutants. Orange, purple, green, and sky-blue squares denote APSES, coiled-coil, homologous to apolipoprotein, and transmembrane (TM) domains, respectively.

b. Spot assay of Bqt4-deletion mutants (shown in **a)** as indicated on the left (full-length (FL), Δ1-140, Δ141-262 and Δ259-383; minus (-) indicates GFP only). The GFP-tagged Bqt4 mutants were expressed in the *lem2* shut-off *bqt4*Δ cells, which are synthetic lethal upon thiamine addition. WT represents the wild-type *S. pombe* strain. Five-fold serially diluted cells were spotted on EMMG plates in the absence (-thiamine) or presence (+thiamine) of thiamine, and growth of these cells was observed after 3 days.

c. Localization of the Bqt4 fragments shown in **a**. GFP-Bqt4 and mCherry-Bqt3 were co-expressed and observed. The scale bar represents 5 µm.

d. Schematic diagrams of Bqt4-deletion mutants at amino acid residues 340-383. The 364-383 aa region was named KSE.

e. Spot assay of the Bqt4-deletion mutants shown in **d**. GFP-Bqt4 fragments indicated on the left were expressed in the *lem2* shut-off *bqt4*Δ cells, and the growth of these cells was observed as described in **b**.

f. Localization of the Bqt4 fragments shown in **d**. GFP-Bqt4 fragments and mCherry-Bqt3 were co-expressed and observed. The scale bar represents 5 µm.

g. Nuclear protein leakage in cells expressing ΔKSE fragment. The *lem2* shut-off *bqt4*Δ cells expressing FL or ΔKSE fragment were cultured in the presence or absence of thiamine and GFP–GST–NLS (nuclear protein marker, green) and Ish1–mCherry (NE marker, magenta) signals were observed using fluorescence microscopy. The scale bar represents 5 µm.

h. Quantification of the nuclear protein leakage phenotype. Fold enrichment of GFP–GST–NLS signal

in the nucleus (nucleus/cytoplasm; N/C) was quantified in three levels according to its leakage: non-leaking (N/C $\geqq$ 10), moderate (10>N/C $\geqq$ 3), and severe (N/C<3). Percentages of the cells were obtained from three independent experiments and the mean with s.d. were plotted as a 100% stacked bar chart. *n* indicates total cell number counted. The statistical significance was assessed using the Chi-square test. **** and n.s. denote $p<0.0001$ and non-significance, respectively.

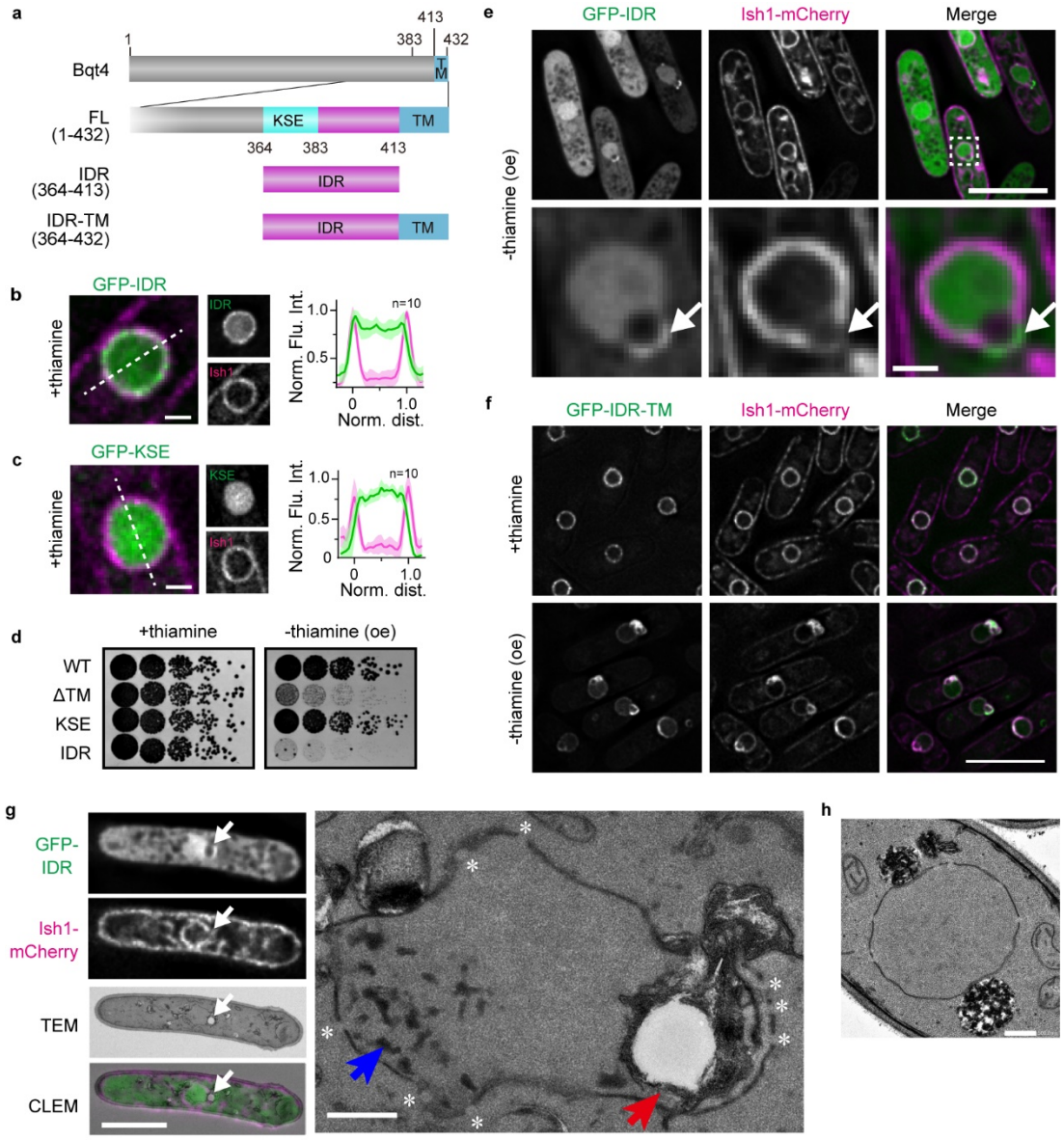

Figure 2. The IDR domain is responsible for maintaining NE structure

a. Schematic diagrams of IDR fragments of Bqt4.

b-c. Localization of IDR (**b**) and KSE (**c**) fragments. GFP-IDR or KSE fragments (green) were expressed with Ish1-mCherry (magenta). The cells were cultured in the presence of thiamine and then observed using fluorescence microscopy (left panels). The scale bars represent 1 μm. Quantifications of their localization are shown on the right. Fluorescence intensities of Bqt4 fragments and Ish1 on the white-dashed line were quantified. The normalized mean values calculated from 10 nuclei were plotted with standard deviation along the normalized nuclear size — 0 and 1 represent the NE at both sides of the nucleus.

d. Spot assay of the cells overexpressing the IDR fragment. GFP-Bqt4 fragments indicated on the left were expressed under the *nmt1* promoter. The growth of the cells was observed as described in Fig. 1**b**. oe represents overexpression.

e. Localization of overexpressed IDR. GFP-IDR (green) was overexpressed in cells with Ish1-mCherry (magenta) and the localization was observed using fluorescence microscopy. The dashed

square region is enlarged at the bottom. The scale bars in the top and bottom panels represent 5 and 1 μm, respectively. Arrows indicate the herniated NE.

f. Localization of IDR-TM. GFP-IDR-TM (green) was expressed in cells with Ish1-mCherry (magenta). The cells were cultured in EMMG with (+thiamine) or without (-thiamine (oe)) thiamine and the localization of IDR-TM was observed using fluorescence microscopy. The scale bar represents 5 μm.

g-h. Representative CLEM images of the cells overexpressing IDR. Cells overexpressing IDR were observed using fluorescence microscopy, followed by a transmission electron microscope (TEM, left). The CLEM image is shown on the left bottom. White arrows indicate a herniated NE observed in the fluorescence image. The magnified TEM image around the nucleus is shown on the right. Red and blue arrows indicate the vacuole-like structure surrounded by a multi-layer membrane and electron-dense patches, respectively. Asterisks indicate NPC. The TEM image of wild-type cells is shown in **h**. The scale bars in left and right panels in **g**, and in **h** represent 5 μm, 500 nm, and 500 nm, respectively.

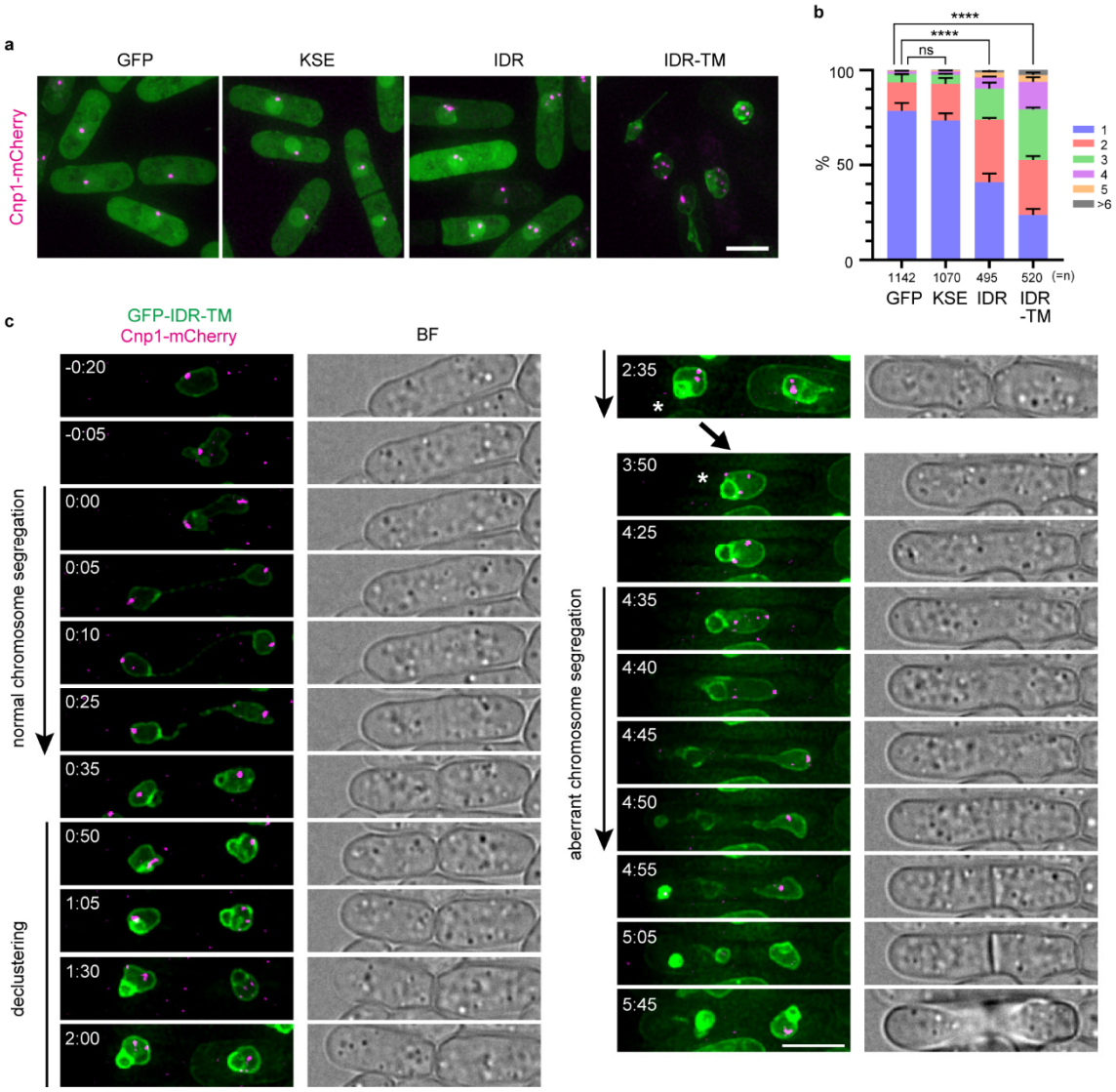

Figure 3. Overexpression of the IDR region disturbs centromere clustering

a. Subcellular localization of centromeres in cells overexpressing the IDR fragments. The CENP-A homolog Cnp1 was expressed as an mCherry-tagged protein (magenta) in cells overexpressing Bqt4 fragments, and its localization was observed using fluorescence microscopy. Scale bar represents 10 µm.

b. Quantification of centromere number. The number of centromeres in each nucleus was counted and plotted as a 100% stacked bar chart. The statistical significance was assessed using the Chi-square test. **** denote $p<0.0001$.

c. Time-lapse imaging. Cells harboring Cnp1-mCherry and *nmt1*-driven GFP-IDR-TM were cultured in EMMG supplemented with 1 µM YAM2 for overnight. After washing out YAM2, the cells were observed using microscopy every 5 min. Elapsed times (h:min) are relative to the onset of first mitosis. The cell labeled by an asterisk (Time 2:35) is shown for the second mitosis (from 3:50 to 5:45). BF denotes a bright-field image. The scale bar represents 5 µm.

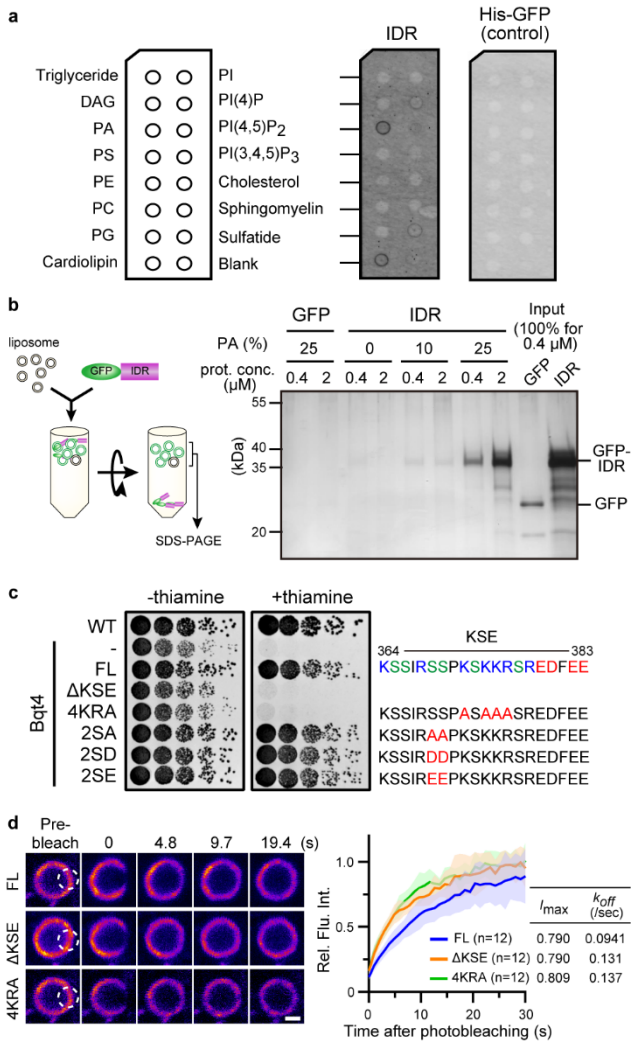

Figure 4. Bqt4 directly binds to PA via IDR

a. Lipid binding assay. The schematic illustration on the left shows lipids spotted on the membrane lipid strip. His-GFP-IDR or His-GFP was incubated with the membrane and the bound protein was detected using fluorescence.

b. Liposome-binding assay. The left diagram shows the procedure of the assay. Liposomes generated from a defined percentage of phospholipids were mixed with GFP or GFP-IDR and then separated via density gradient centrifugation. The protein-liposome complex visualized through light scattering was collected and subjected to SDS-PAGE. Protein components were detected using silver staining. The bound proteins are shown in the right panel.

c. Spot assay of the point mutants in the KSE region. The cells expressing Bqt4 point mutants shown on the left were spotted and the growth was observed as described in Fig. 1b. The mutation sites in the KSE region are shown on the right.

d. FRAP analysis of GFP-tagged Bqt4 fragments (FL, ΔKSE and 4KRA). The dashed white open circle region was bleached, and the recovery of fluorescence intensity after bleaching in the circle was measured. Solid lines in the FRAP curve indicate the mean value. The areas on both sides of the solid lines indicate standard deviation. The curves were fitted as a single exponential association, and the maximum recovery rate (I_{max}) and dissociation coefficient (k_{off}) are shown on the right. The scale bar represents 1 μm.

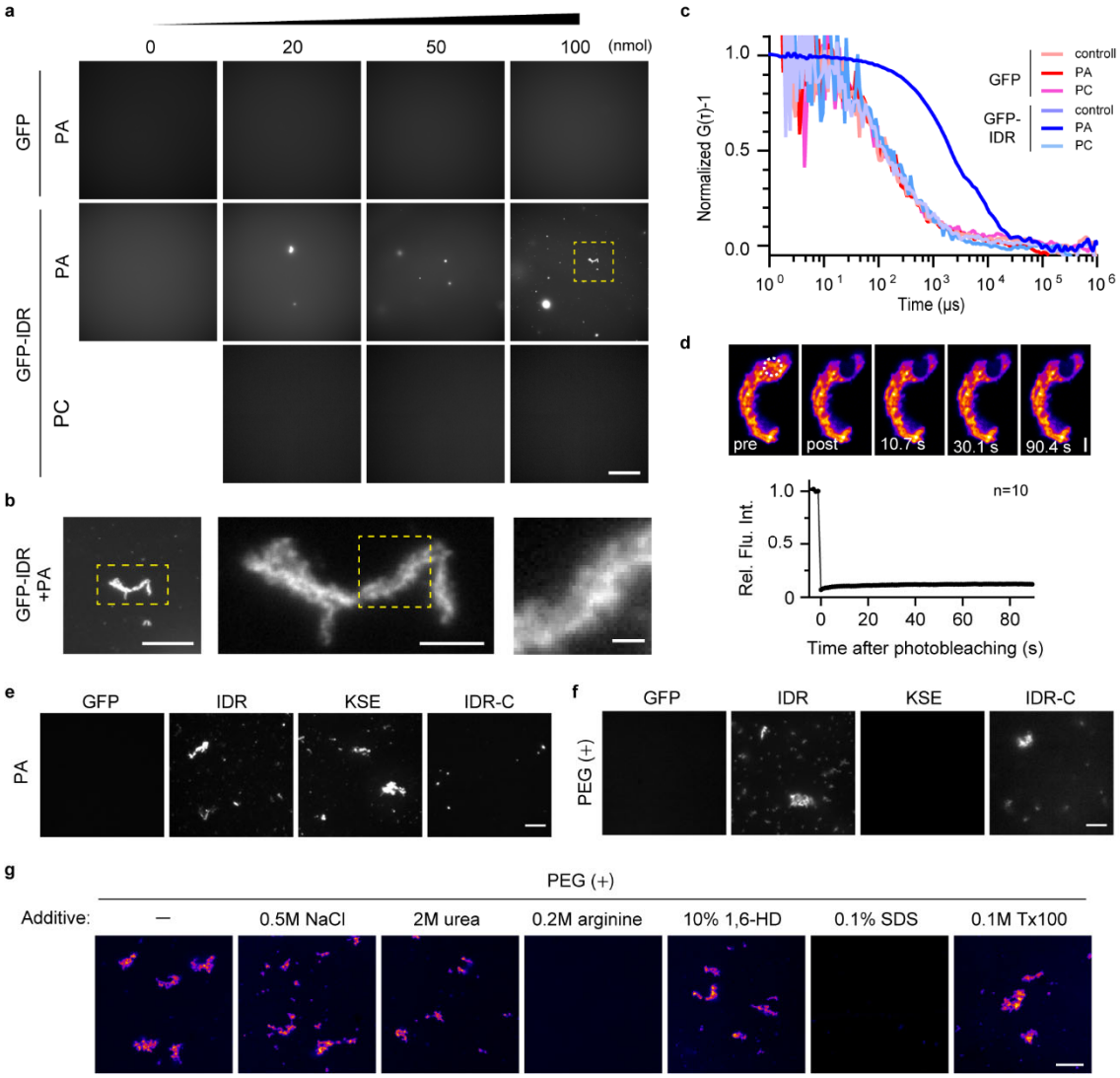

Figure 5. IDR forms solid aggregate with PA

a-b. Aggregate formation of GFP-IDR with PA. Purified GFP and GFP-IDR were mixed with increased amounts (0, 20, 50, and 100 nmol) of PA or PC. The aggregates formed were observed using fluorescence microscopy (**a**). The yellow-squared region is enlarged in (**b**). The scale bar in (**a**) represents 50 μm. Scale bars in (**b**) represent 20, 5, and 1 μm from left to right, respectively.

c. Molecular clustering state of GFP-IDR aggregates. GFP (left) and GFP-IDR (right) were mixed with 100 nmol PA or PC, and then the mixture was analyzed using FCS. Count rate and normalized auto-correlation function calculated from the measurement (G(τ)) are shown in (**c**) and (**d**), respectively. Inlets in (**c**) are enlarged images of the part of the count rate.

d. Molecular exchange rate in GFP-IDR aggregate. GFP-IDR was mixed with 100 nmol PA, and the molecular exchange rate of the formed aggregate was measured using FRAP. The white-dashed circle denotes the bleached region. The scale bar represents 2 μm. The fluorescence recovery curve shows mean ± s.e.m. from ten measurements.

e. Responsible region of aggregate formation in the IDR with PA. GFP, GFP-IDR (IDR), GFP-KSE (KSE), and GFP-IDR-C (IDR-C) were mixed with 100 nmol PA, and the formed aggregate was observed using fluorescence microscopy. The scale bar represents 10 μm.

f. Responsible region of aggregate formation in the IDR under crowding conditions. GFP, GFP-IDR (IDR), GFP-KSE (KSE), and GFP-IDR-C (IDR-C) were incubated in a crowding buffer containing 5% PEG as a crowder, and the formed aggregate was observed using fluorescence microscopy. The

scale bar represents 10 μm.

g. Effect of additives on the aggregate formation. GFP-IDR was incubated in a crowding buffer supplied with additives indicated on the top, and the formed aggregate was observed using fluorescence microscopy. The scale bar represents 10 μm.

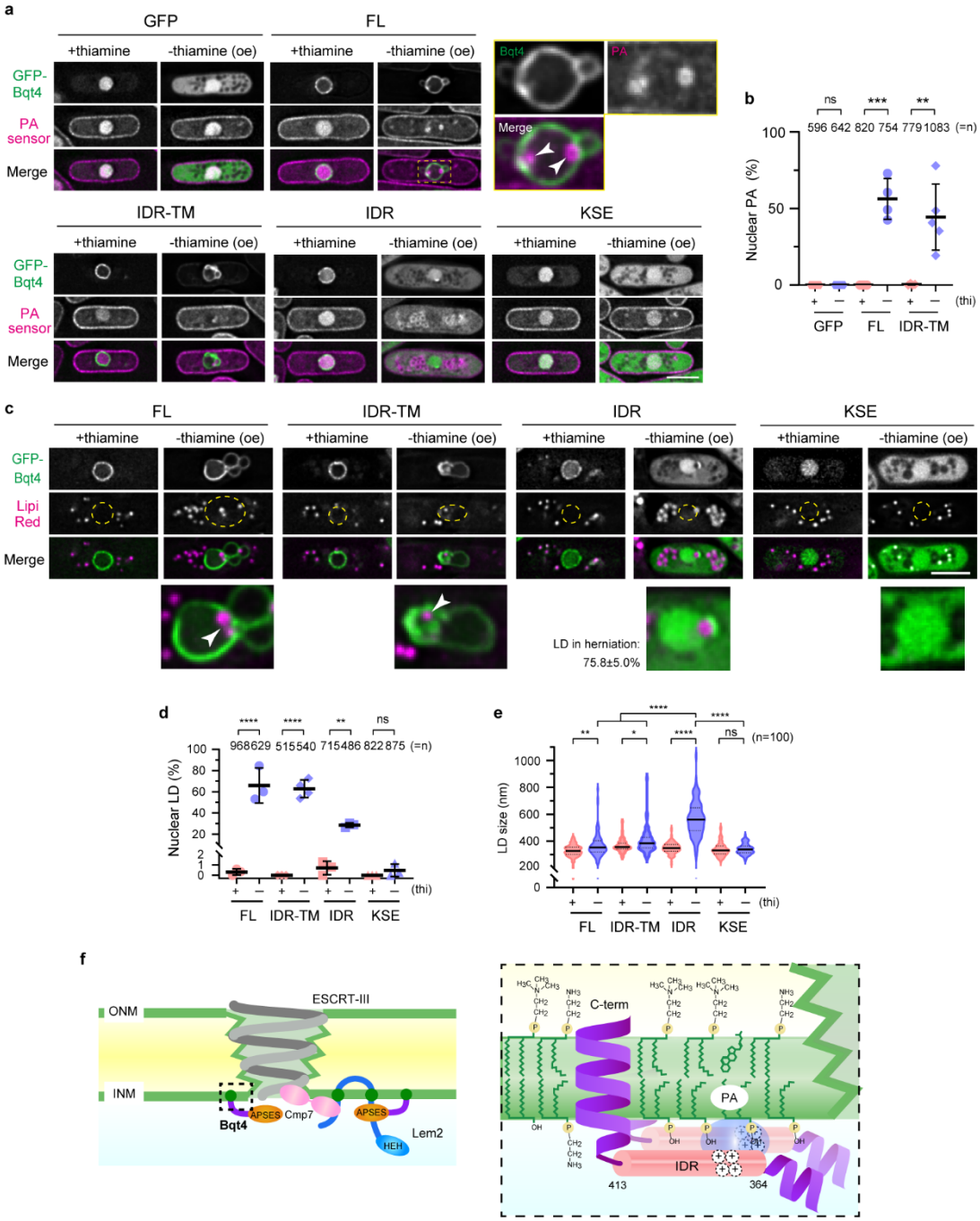

Figure 6. Overexpression of IDR disturbs intracellular lipid distribution

a. Visualization of PA in cells overexpressing Bqt4 fragments. The mCherry-tagged PA sensor based on *S. cerevisiae* Opi1 was expressed in *S. pombe* cells. The Bqt4 fragments indicated on the top were overexpressed by culturing the cells in EMMG medium in the presence or absence of thiamine (labeled "+thiamine" and "-thiamine (oe)", respectively). The dashed yellow square region in FL is enlarged at the right. Arrowheads indicate the PA-enriched region at the NE. The scale bar represents 5 µm.

b. Quantification of the cells containing nuclear phosphatidic acid (PA). Percentage of the cells containing a nuclear PA in (**a**) was determined from three to five independent experiments. The horizontal bold lines and whiskers represent the mean and standard deviation, respectively. The statistical significance was assessed using unpaired two-tailed Student's *t*-test. *** and ** denote

$p<0.001$ and $p<0.01$, respectively. ns denotes not significant. Total cell numbers counted (n) are shown on the top.

c. Intracellular distribution of lipid droplet (LD). Cells overexpressing the Bqt4 fragments were stained with an LD stainer, LipiRed, and the subcellular localization was observed using fluorescence microscopy. Yellow circles indicate nuclear position. Arrowheads indicate nuclear LD. The scale bar represents 5 μm.

d. Quantification of the cells containing a nuclear LD. Percentage of the cells containing a nuclear LD in (**c**) was determined from three or four independent experiments. The horizontal bold lines and whiskers represent the mean and standard deviation, respectively. The statistical significance was assessed using one-way ANOVA, followed by Tukey's test. **** and ** denote $p < 0.0001$ and $p < 0.01$, respectively. ns denotes not significant. Total cell numbers counted (n) are shown on the top.

e. Quantification of LD size. The size of LDs observed in (**b**) was measured as follows: measure the line profile of each LD, fit the profile as Gaussian, and then calculate the full width of half maximum (FWHM) of the LD. The FWHM of 100 LDs from at least five cells was measured and plotted as a violin plot. The horizontal bold and dotted lines indicate the median and quartiles, respectively. The statistical significance was assessed using one-way ANOVA, followed by Tukey's test. ****, ** and * denote $p < 0.0001$, $p < 0.01$and $p < 0.05$, respectively. ns denotes not significant.

f. Working model. Bqt4 potentially supports NE sealing via two distinct pathways by accumulating PA to the INM. First, Bqt4 generates a preferable micro membrane environment for robust ESCRT-III loading. Bqt4 can enrich PA and Lem2, both of which facilitate and stabilize Cmp7 loading to the NE rupture sites. Second, Bqt4 supplies phospholipids by controlling the balance of lipid synthesis in the INM. Hence, Bqt4 has a broad role in NE maintenance.

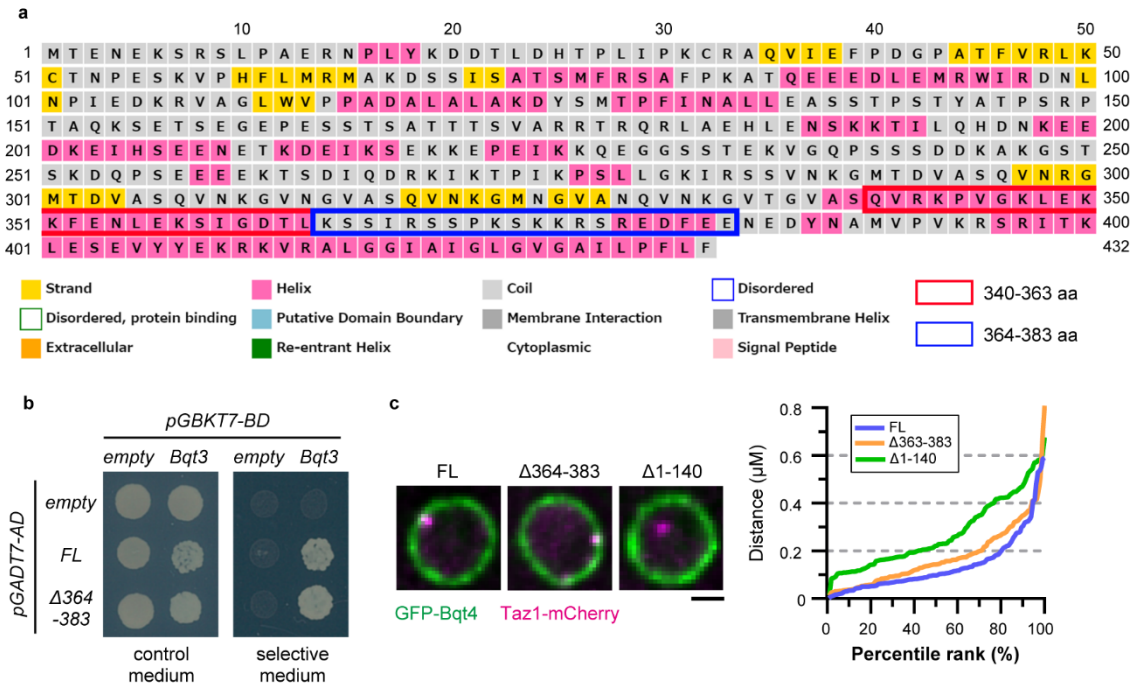

Supplementary Fig. S1 KSE region characteristics

a. Secondary structure prediction of Bqt4 by PSIPRED 4.0. The sequences surrounded by red and blue frames indicate 340-363 aa and 364-383 aa, respectively.

b. Yeast two-hybrid assay. *S. cerevisiae* cells expressing the full-length Bqt4 (FL) and the Bqt4 Δ364-383 fragment with Bqt3 were grown on a medium with different auxotrophy (control and selective medium) for 3 days. Fusion proteins with AD (pGADT7-AD) and BD (pGBKT7-BD) are shown on the left and top, respectively.

c. Distance between the NE and telomeres. (Left) Full-length (FL) and fragments (Δ364-383 and Δ1-140) of Bqt4 tagged with GFP (green) were co-expressed with Taz1-mCherry as a maker for telomere (magenta). (Right) Distance between the NE to telomeres was measured and plotted as a percentile rank. The scale bar represents 1 μm.

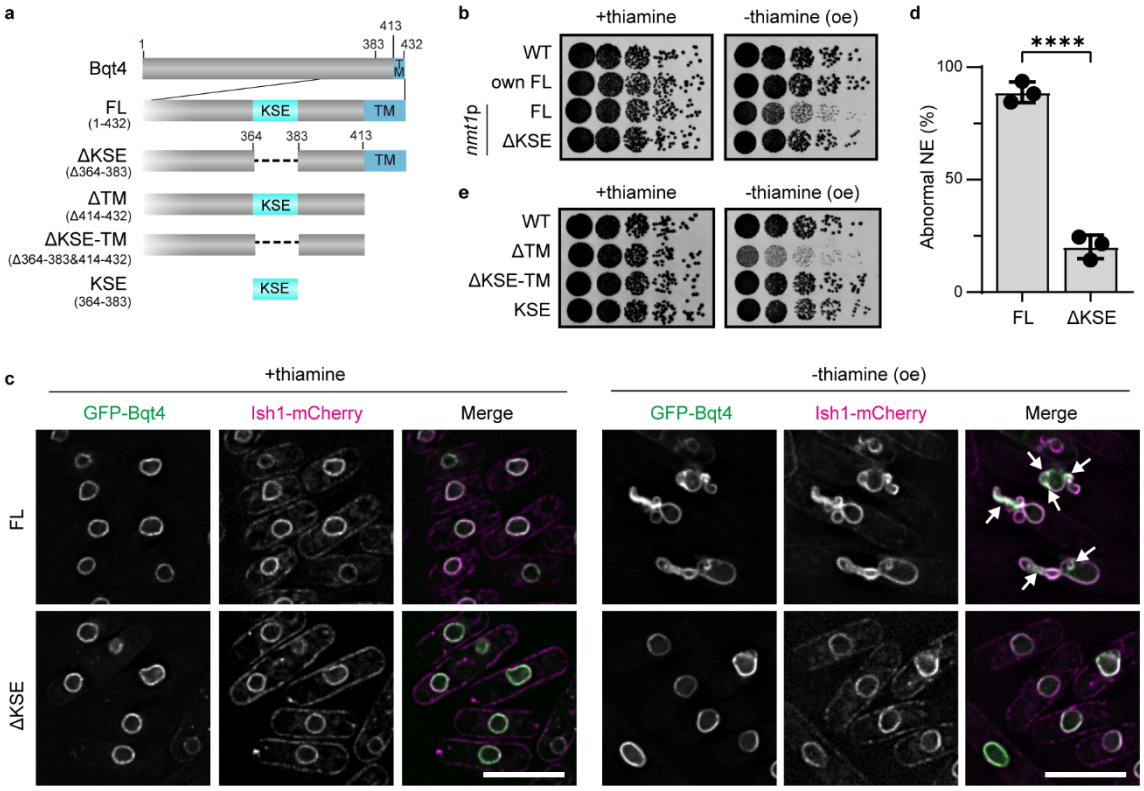

Supplementary Fig. S2. The KSE region is required for cell growth, but insufficient for dominant negative defects

a. Schematic diagrams of KSE fragments. TM denotes the transmembrane domain.

b. Spot assay of the cells overexpressing ΔKSE fragment. GFP-tagged Bqt4 fragments indicated on the left were expressed under authentic (own) or *nmt1* (*nmt1p*) promoters. The growth of the cells was observed as described in Fig. 1**a**. oe represents overexpression.

c. NE deformation by Bqt4 overexpression. GFP-tagged FL or ΔKSE were expressed with Ish1-mCherry as a nuclear membrane marker (Asakawa et al., 2022) in *S. pombe* cells. The cells were cultured in the EMMG medium with or without thiamine (labeled "+thiamine" and "-thiamine (oe)," respectively), and then observed using fluorescence microscopy. Arrows indicate the region of Bqt4 enrichment. The scale bars represent 5 µm.

d. Quantification of abnormal NE morphology. Percentage of the cells that showed abnormal NE morphology in (**c**) was quantified from three independent experiments. The mean and standard deviation were shown. The statistical significance was assessed using two-tailed Welch's *t*-test. **** denotes $p < 0.0001$.

e. Spot assay of cells overexpressing the Bqt4 fragments. GFP-Bqt4 fragments indicated on the left were expressed under the *nmt1* promoter. The growth of the cells was observed as described in **c**.

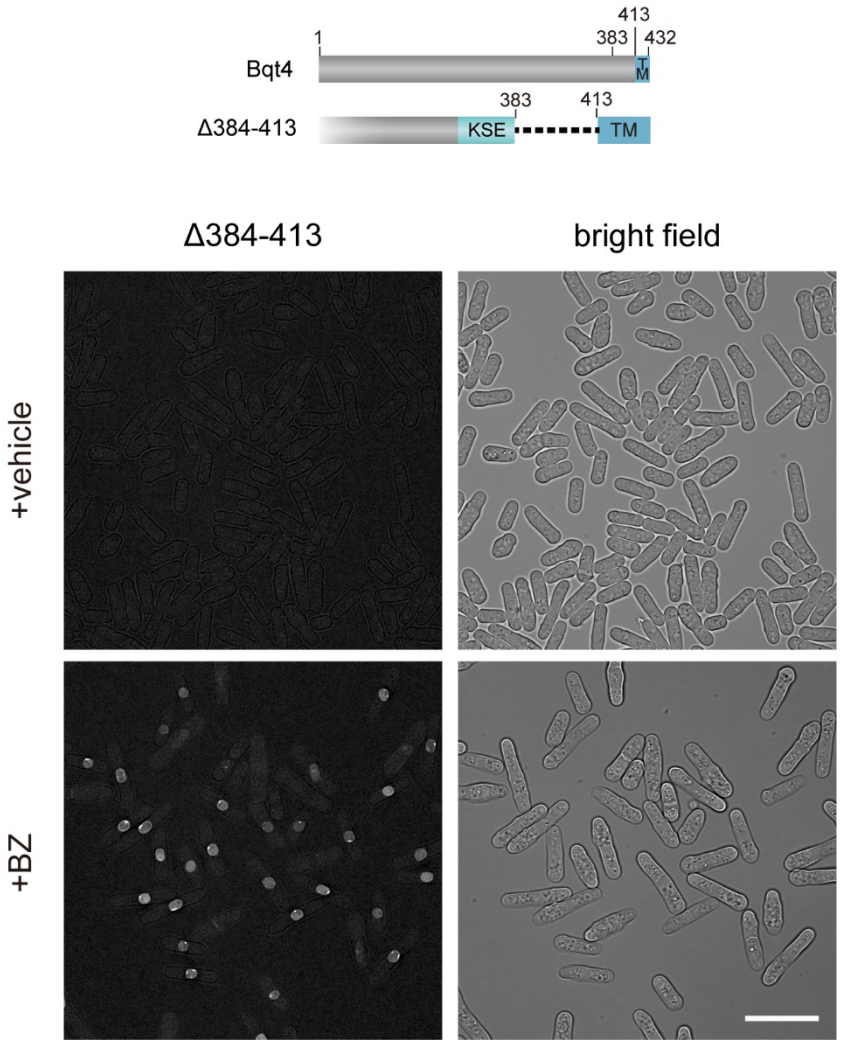

Supplementary Fig. S3 Bqt4Δ384-413 protein fragment undergoes degradation
Green fluorescent protein (GFP)-tagged Bqt4Δ384-413 fragment was expressed in the *lem2*-shut-off *bqt4*Δ cells and observed in the presence (+BZ) or absence (+vehicle) of 1mM bortezomib, a proteasome inhibitor effective in *Schizosaccharomyces pombe* cells. Bright-field images are shown on the right side. Scale bar represents 20 µm.

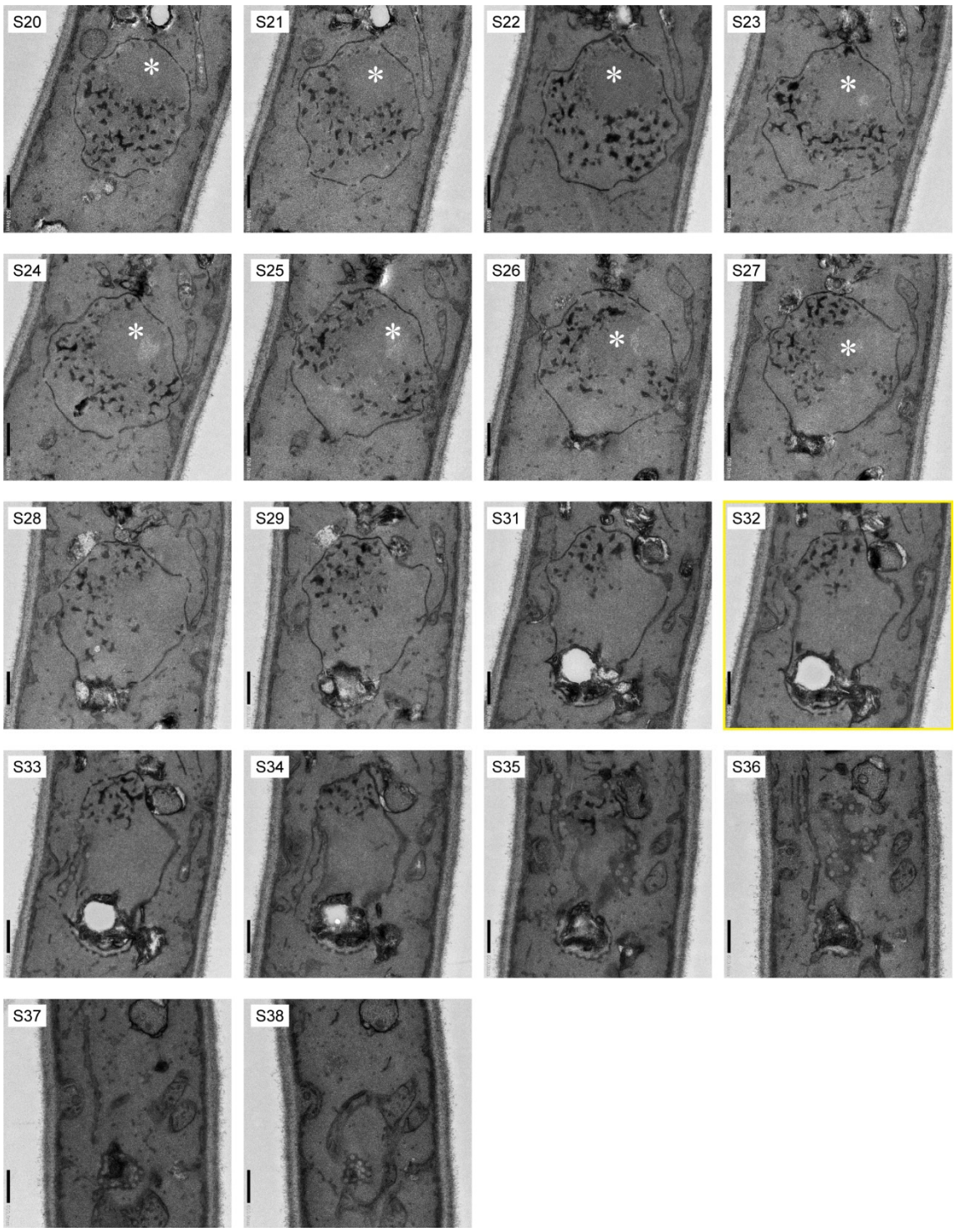

Supplementary Fig. S4 Serial section TEM images of the cell overexpressing IDR
Serial-section TEM images of cells overexpressing IDR are shown in Fig. 3**g**. The numbers on the upper left indicate the section numbers. S32 is shown in Fig. 3**g**. Asterisk at S20-S27 indicates the nucleolus. The scale bars represent 500 nm.

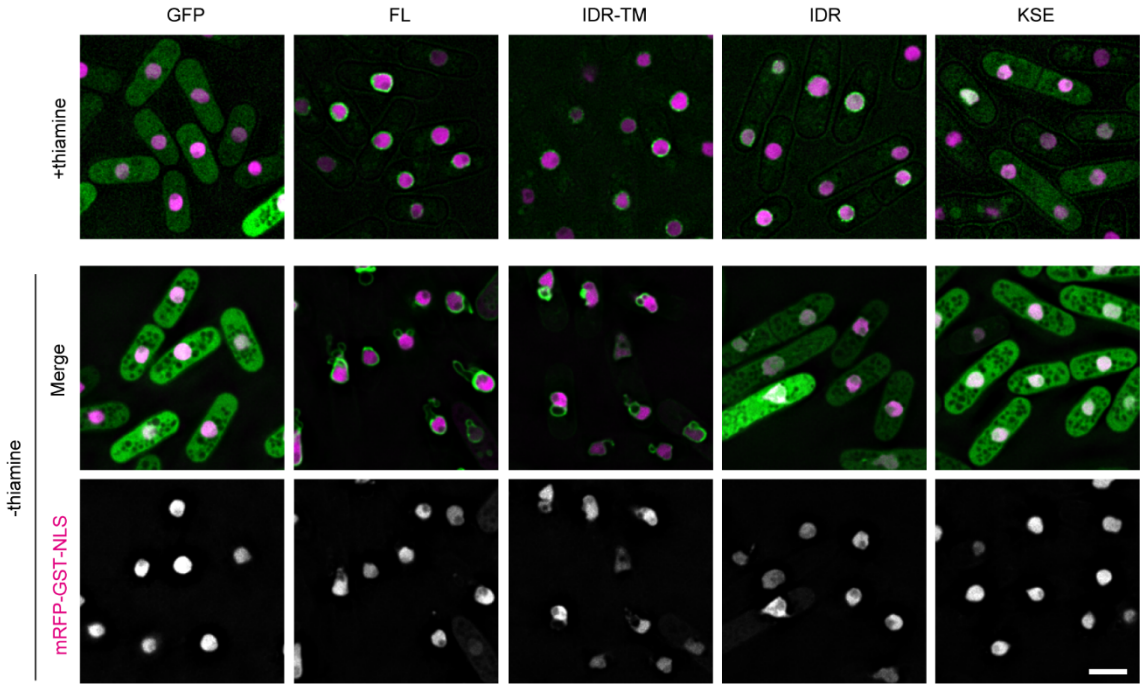

Supplementary Fig. S5 Overexpression of Bqt4 fragments did not disturb the NE integrity
Cells expressing Bqt4 fragments and mRFP-GST-NLS were cultured in the presence or absence of thiamine and observed using fluorescence microscopy. Scale bar represents 5 µm.

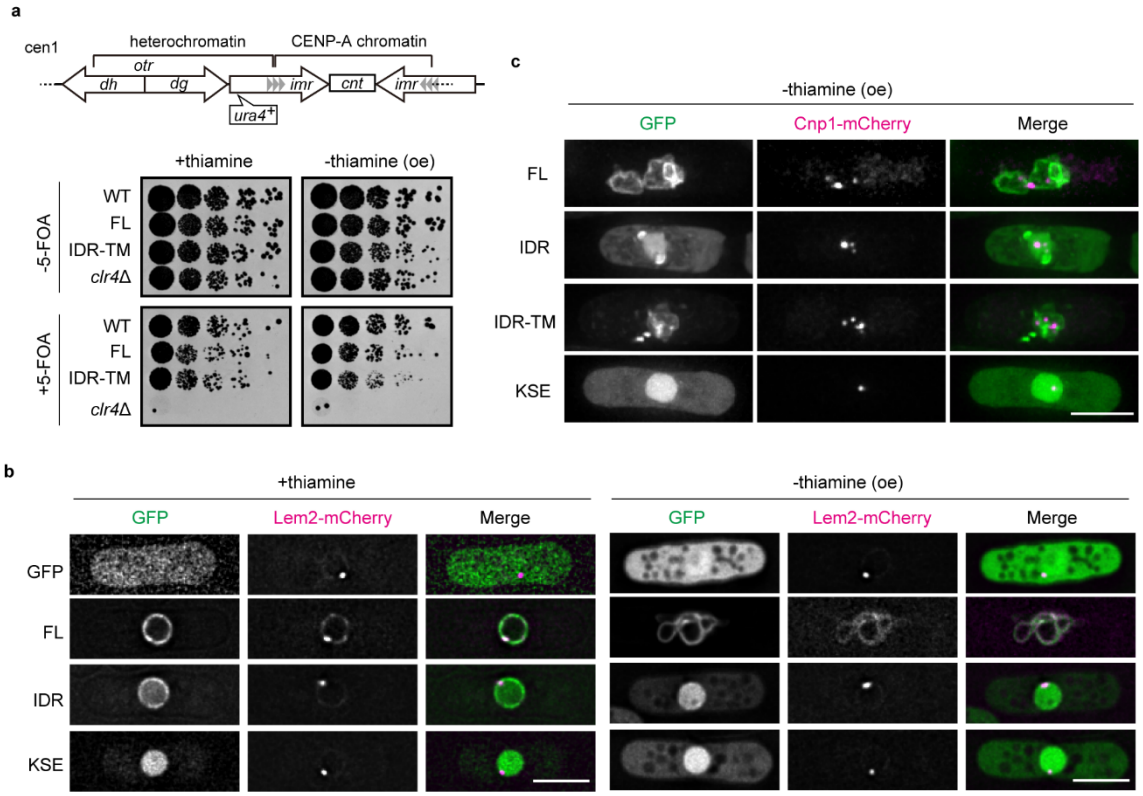

Supplementary Fig. S6 Lem2 did not involve centromeric defects caused by Bqt4 overexpression
a. Heterochromatin silencing assay in cells overexpressing GFP-FL or IDR-TM. The cells with increased expression of GFP-FL or -IDR-TM and *clr4*Δ cells were spotted on the EMMG containing 5-FOA with or without thiamine in five-fold serial dilutions and then grown at 30°C for 4 days.
b. Subcellular localization of Lem2 in the cells overexpressing Bqt4 fragment. GFP-tagged Bqt4 fragments (green) indicated on the left were expressed in the cells expressing mCherry-tagged Lem2 (Lem2-mCherry, magenta). The cells were cultured in the EMMG medium in the presence or absence of thiamine ("+thiamine" and "-thiamine (oe)", respectively). Lem2-mCherry is accumulated at the centromere in the control cells disrupted for the authentic *bqt4*$^{+}$ gene as previously reported (Hirano et al., 2018). The scale bars represent 5 µm.
c. Distribution of centromeres in *lem2*Δ cells. *lem2*Δ cells expressing the GFP or GFP-Bqt4 fragments indicated on the left (green) and Cnp1-mCherry (magenta) were cultured in EMMG medium and observed using fluorescence microscopy. The scale bar represents 5 µm.

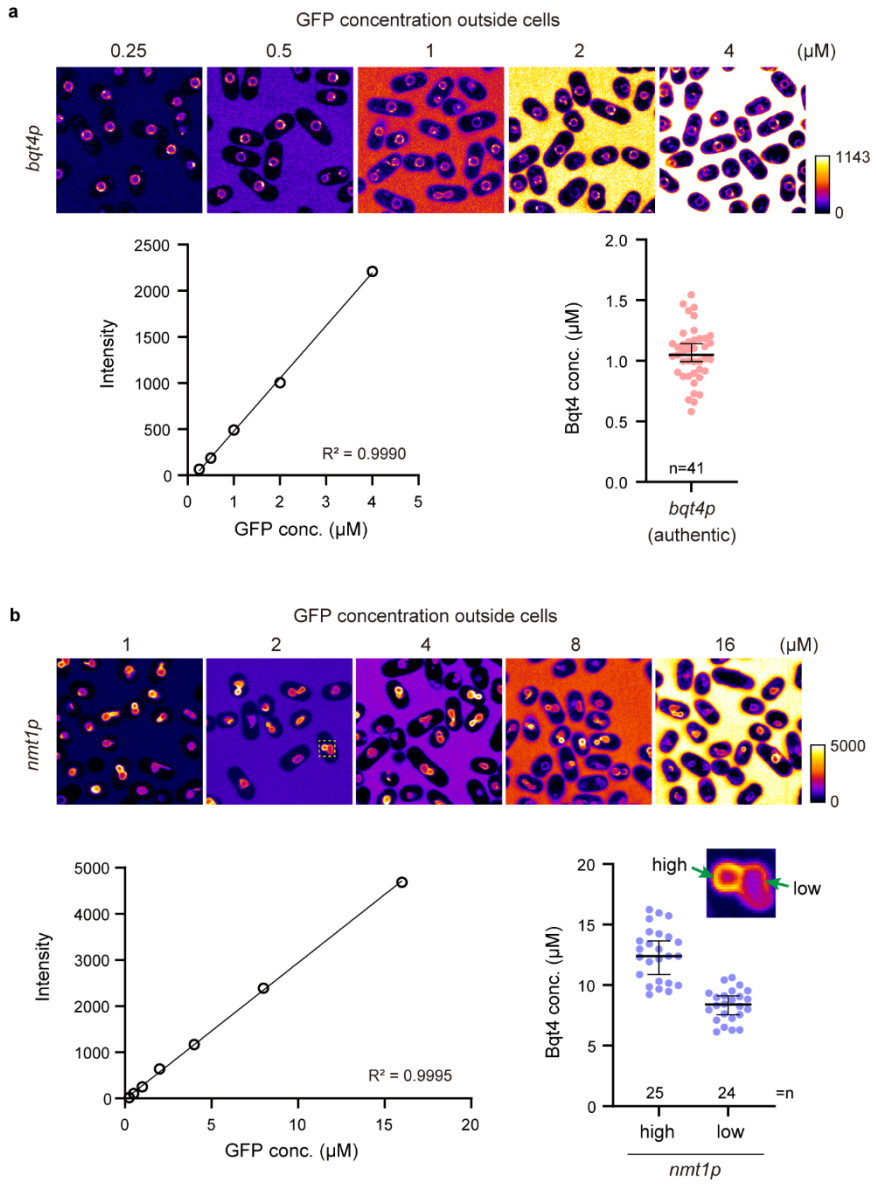

Supplementary Fig. S7 Bqt4 concentration in the NE

Cells expressing GFP-Bqt4 under authentic (**a**) or *nmt1* (**b**) promoters were mixed with purified GFP solutions of increasing concentrations indicated on the top and observed using fluorescence microscopy (top panels). A standard curve was constructed by quantifying the intensities outside of the cells (bottom left). Bqt4 concentrations in the NE were determined using a standard curve (bottom right). Since the Bqt4 concentration in the NE expressed under the *nmt1* promoter was not uniform, we categorized it into high- and low-concentration regions (inset of (**b**)). The horizontal line and whiskers in the plots denote median and 95% confidence intervals.

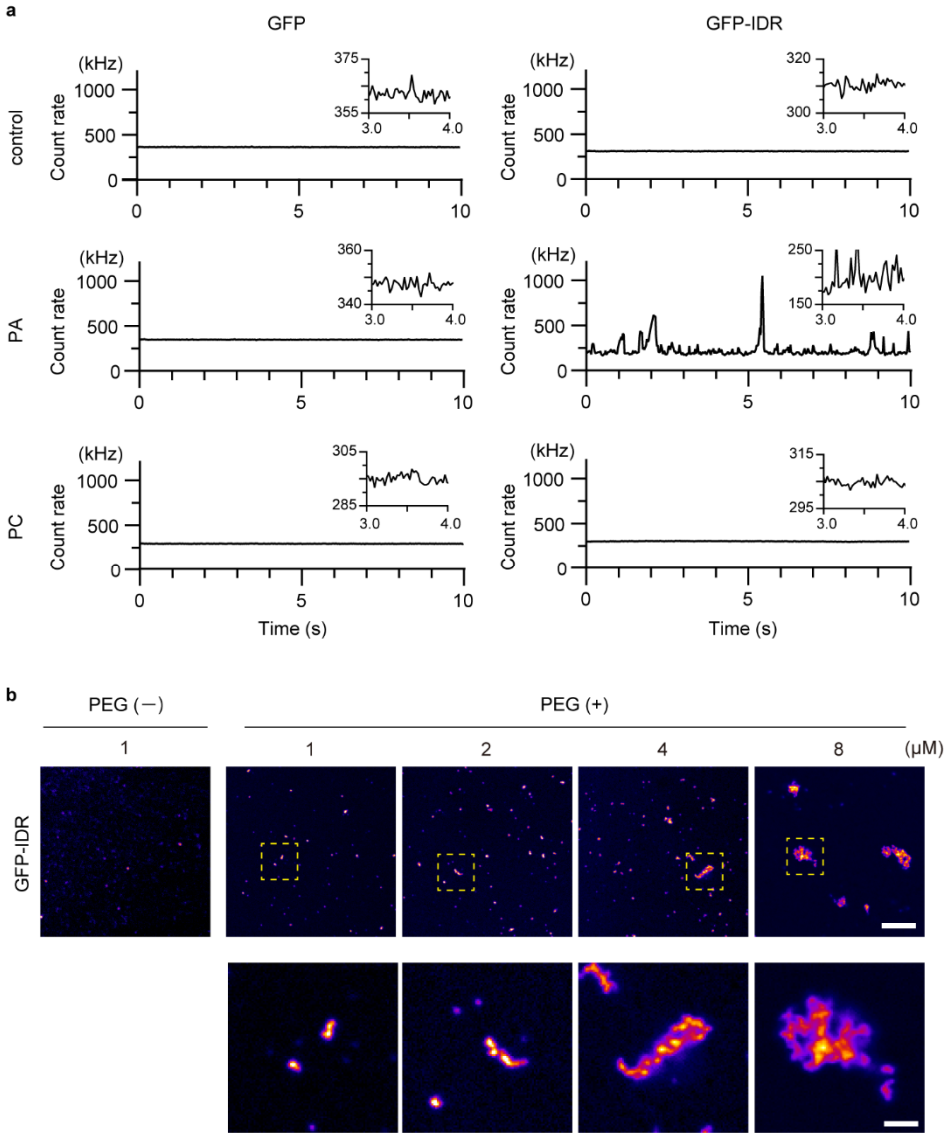

Supplementary Fig. S8 Molecular clustering of GFP-IDR

a. Fluorescence intensity fluctuation during FCS measurements. GFP (left) and GFP-IDR (right) were mixed with 100 nmol PA or PC, and then the mixture was analyzed using FCS. Inlets are enlarged images of the part of the count rate.

b. Concentration dependency of the aggregate formation of GFP-IDR. Increasing concentrations of GFP-IDR indicated on the top were incubated in a crowding solution in the presence or absence of 5% PEG ("PEG(+)" and "PEG(-)"). The formed aggregates were observed using a fluorescence microscope. The yellow dashed square regions are enlarged at the bottom of the figure. The scale bars in the top and bottom panels indicate 10 and 2 μm, respectively.

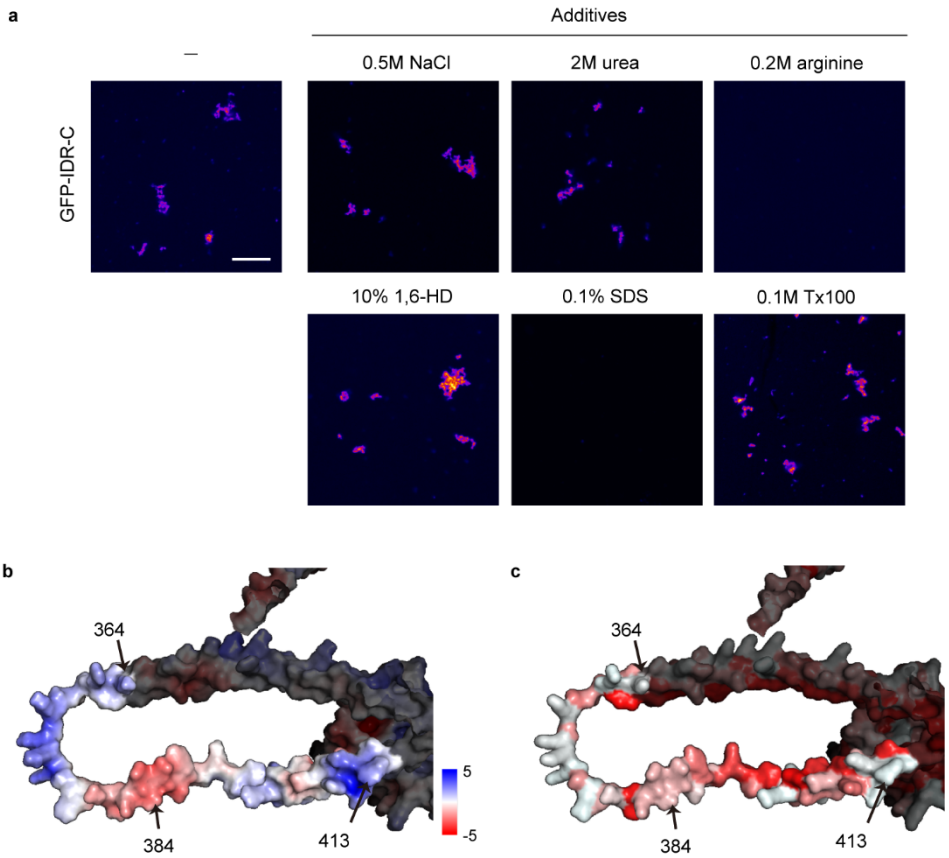

Supplementary Fig. S9 Effect of additives on GFP-IDR-C aggregate

a. Eight micromolar of GFP-IDR-C was incubated in a crowding solution supplied with additives indicated on the top, and the formed aggregates were observed using fluorescence microscopy. The scale bar represents 10 µm.

b. Electrostatics of IDR. The electrostatic condition of Bqt4 was calculated by the adaptive Poisson-Boltzmann solver plugin in PyMOL software and drawn on the predicted Bqt4 structure by Alphafold2 (O60158). The blue and red portions indicate amino acid residues with positive and negative charges, respectively. Bright residues correspond to 364-413 aa.

c. Hydrophobicity of IDR. Hydrophobicity around IDR is shown on the predicted Bqt4 structure as in (**b**). The red and white portions indicate hydrophobic and hydrophilic regions, respectively.

Supplementary Table 1. Yeast strains used in this study

S. pombe strains

Strain	Genotype	Source	Figure
h-972	*h⁻*	Laboratory stock	1b, e, 2d, h, 4c, S2b, e
H1N1198	*h⁻ leu1⁺::nmt81p-FLAG-lem2-IAA17-HA lem2Δ::kan^r bqt4Δ::hph lys1⁺::GFP*	This study	1b, e, 4c
H1N2050	*h⁻ leu1⁺::nmt81p-FLAG-lem2-IAA17-HA lem2Δ::kan^r bqt4Δ::hph lys1⁺::bqt4p-GFP-bqt4*	This study	1b, e, 4c, d
H1N1203	*h⁻ leu1⁺::nmt81p-FLAG-lem2-IAA17-HA lem2Δ::kan^r bqt4Δ::hph lys1⁺::GFP-bqt4(Δ1-140aa)*	This study	1b
H1N2051	*h⁻ leu1⁺::nmt81p-FLAG-lem2-IAA17-HA lem2Δ::kan^r bqt4Δ::hph lys1⁺::bqt4p-GFP-bqt4(Δ141-262aa)*	This study	1b
H1N2055	*h⁻ leu1⁺::nmt81p-FLAG-lem2-IAA17-HA lem2Δ::kan^r bqt4Δ::hph lys1⁺::bqt4p-GFP-bqt4(Δ259-383aa)*	This study	1b
H1N2115	*h⁻ bqt4Δ:: kan^r bqt3Δ::NAT aur1r⁺::mCherry-bqt3 lys1⁺::bqt4p-GFP-bqt4*	This study	1c
H1N2243	*h⁻ bqt4Δ:: kan^r bqt3Δ::NAT aur1r⁺::mCherry-bqt3 lys1⁺::bqt4p-GFP-bqt4(Δ1-140aa)*	This study	1c
H1N2116	*h⁻ bqt4Δ:: kan^r bqt3Δ::NAT aur1r⁺::mCherry-bqt3 lys1⁺::bqt4p-GFP-bqt4(Δ141-262aa)*	This study	1c
H1N2120	*h⁻ bqt4Δ:: kan^r bqt3Δ::NAT aur1r⁺::mCherry-bqt3 lys1⁺::bqt4p-GFP-bqt4(Δ259-383aa)*	This study	1c
H1N2056	*h⁻ leu1⁺::nmt81p-FLAG-lem2-IAA17-HA lem2Δ::kan^r bqt4Δ::hph lys1⁺::bqt4p-GFP-bqt4(Δ340-383aa)*	This study	1e
H1N2057	*h⁻ leu1⁺::nmt81p-FLAG-lem2-IAA17-HA lem2Δ::kan^r bqt4Δ::hph lys1⁺::bqt4p-GFP-bqt4(Δ340-363aa)*	This study	1e
H1N2058	*h⁻ leu1⁺::nmt81p-FLAG-lem2-IAA17-HA lem2Δ::kan^r bqt4Δ::hph lys1⁺::bqt4p-GFP-bqt4-ΔKSE(Δ364-383aa)*	This study	1e, 4c, d
H1N2121	*h⁻ bqt4Δ:: kan^r bqt3Δ::NAT aur1r⁺::mCherry-bqt3 lys1⁺::bqt4p-GFP-bqt4(Δ340-383aa)*	This study	1f
H1N2122	*h⁻ bqt4Δ:: kan^r bqt3Δ::NAT aur1r⁺::mCherry-bqt3 lys1⁺::bqt4p-GFP-bqt4(Δ340-363aa)*	This study	1f
H1N2123	*h⁻ bqt4Δ:: kan^r bqt3Δ::NAT aur1r⁺::mCherry-bqt3 lys1⁺::bqt4p-GFP-bqt4-ΔKSE (Δ364-383aa)*	This study	1f
H1N2802	*h⁻ ura4-D18 leu1⁺::adh1p-GFP-GST-NLS ish1-mCherry::ura4⁺ lys1⁺::nmt81p-FLAG-lem2-IAA17-HA lem2Δ::kan^r bqt4Δ::hph aur1^r::pYC19*	This study	1g, h
H1N2803	*h⁻ ura4-D18 leu1⁺::adh1p-GFP-GST-NLS ish1-mCherry::ura4⁺ lys1⁺::nmt81p-FLAG-lem2-IAA17-HA lem2Δ::kan^r bqt4Δ::hph aur1^r:: bqt4p-bqt4*	This study	1g, h
H1N2804	*h⁻ ura4-D18 leu1⁺::adh1p-GFP-GST-NLS ish1-mCherry::ura4⁺ lys1⁺::nmt81p-FLAG-lem2-IAA17-HA lem2Δ::kan^r bqt4Δ::hph aur1^r:: bqt4p-bqt4ΔKSE(Δ364-383aa)*	This study	1g, h
H1N2034	*h⁻ bqt4Δ::hph Ish1⁺-mCherry::bsd lys1⁺::nmt1p-GFP-bqt4-IDR(364-413aa)*	This study	2b, d, e, g, S4
H1N2615	*h⁻ bqt4Δ::hph Ish1⁺-mCherry::bsd lys1⁺::nmt1p-GFP-bqt4-KSE(364-383aa)*	This study	2c, d, S2e
H1N1852	*h⁻ bqt4Δ::hph Ish1⁺-mCherry::bsd lys1⁺::nmt1p-GFP-bqt4-ΔTM*	This study	2d, S2e
H1N2613	*h⁻ bqt4Δ::hph Ish1⁺-mCherry::bsd lys1⁺::nmt1p-GFP-bqt4-IDRTM(364-432aa)*	This study	2f
H1N2649	*h⁻ bqt4Δ::hph cnp1⁺-FL5-mCherry::kan^r lys1⁺::nmt1p-GFP*	This study	3a, b
H1N2640	*h⁻ bqt4Δ::hph cnp1⁺-FL5-mCherry::kan^r lys1⁺::nmt1p-GFP-bqt4-KSE(364-383aa)*	This study	3 a, b
H1N2641	*h⁻ bqt4Δ::hph cnp1⁺-FL5-mCherry::kan^r lys1⁺::nmt1p-GFP-bqt4-IDR(364-413aa)*	This study	3 a, b
H1N2737	*h⁻ bqt4Δ::hph cnp1⁺-FL5-mCherry::kan^r lys1⁺::nmt1p-GFP-bqt4-IDRTM(364-432aa)*	This study	3 a-c, M1
H1N2155	*h⁻ leu1⁺::nmt81p-FLAG-lem2-IAA17-HA lem2Δ::kan^r bqt4Δ::hph lys1⁺::bqt4p-GFP-bqt4-2SA*	This study	4c
H1N2156	*h⁻ leu1⁺::nmt81p-FLAG-lem2-IAA17-HA lem2Δ::kan^r bqt4Δ::hph lys1⁺::bqt4p-GFP-bqt4-2SD*	This study	4c
H1N2157	*h⁻ leu1⁺::nmt81p-FLAG-lem2-IAA17-HA lem2Δ::kan^r bqt4Δ::hph lys1⁺::bqt4p-GFP-bqt4-2SE*	This study	4c
H1N2158	*h⁻ leu1⁺::nmt81p-FLAG-lem2-IAA17-HA lem2Δ::kan^r bqt4Δ::hph lys1⁺::bqt4p-GFP-bqt4-4KRA*	This study	4c, d
H1N2721	*h⁻ lys1⁺::nmt1p-GFP aur1^r::adh11p-2xAH-G120W-mCherry*	This study	6a, b
H1N2722	*h⁻ lys1⁺::nmt1p-GFP-bqt4 aur1^r::adh11p-2xAH-G120W-mCherry*	This study	6a, b

H1N2725	*h⁻ lys1⁺::nmt1p-GFP-bqt4-IDRTM(364-432aa.) aur1ʳ::adh11p-2xAH-G120W-mCherry*	This study	6a, b
H1N2723	*h⁻ lys1⁺::nmt1p-GFP-bqt4-KSE(364-383aa.) aur1ʳ::adh11p-2xAH-G120W-mCherry*	This study	6a
H1N2724	*h⁻ lys1⁺::nmt1p-GFP-bqt4-IDR(364-413aa.) aur1ʳ::adh11p-2xAH-G120W-mCherry*	This study	6a
H1N2716	*h⁻ lys1⁺::nmt1p-GFP-bqt4*	This study	6c-e
H1N2719	*h⁻ lys1⁺::nmt1p-GFP-bqt4-IDRTM(364-432aa.)*	This study	6c-e
H1N2717	*h⁻ lys1⁺::nmt1p-GFP-bqt4-KSE(364-383aa.)*	This study	6c-e
H1N2718	*h⁻ lys1⁺::nmt1p-GFP-bqt4-IDR(364-413aa.)*	This study	6c-e
H1N2078	*h⁻ leu1⁺::nmt81p-FLAG-lem2-IAA17-HA lem2Δ::kanʳ bqt4Δ::hph taz1⁺-mCherry::NAT lys1⁺::bqt4p-GFP*	This study	S1c
H1N2087	*h⁻ leu1⁺::nmt81p-FLAG-lem2-IAA17-HA lem2Δ::kanʳ bqt4Δ::hph taz1⁺-mCherry::NAT lys1⁺::bqt4p-GFP-bqt4(Δ364-383aa)*	This study	S1c
H1N2159	*h⁻ leu1⁺::nmt81p-FLAG-lem2-IAA17-HA lem2Δ::kanʳ bqt4Δ::hph taz1⁺-mCherry::NAT lys1⁺::bqt4p-bqt4(Δ1-140aa)*	This study	S1c
H1N1854	*h⁻ bqt4Δ::hph Ish1⁺-mCherry::bsd lys1⁺::bqt4p-GFP-bqt4*	This study	S2b
H1N1875	*h⁻ bqt4Δ::hph Ish1⁺-mCherry::bsd lys1⁺::nmt1p-GFP-bqt4*	This study	S2b-d, S7b
H1N2124	*h⁻ bqt4Δ::hph Ish1⁺-mCherry::bsd lys1⁺::nmt1p-GFP-bqt4-ΔKSE(Δ364-383aa)*	This study	S2b-d
H1N1992	*h⁻ bqt4Δ::hph Ish1⁺-mCherry::bsd lys1⁺::nmt1p-GFP-bqt4*ΔKSETM*(Δ364-383aa & TM)*	This study	S2e
H1N2377	*h⁻ leu1⁺::nmt81p-FLAG-lem2-IAA17-HA lem2Δ::kanʳ bqt4Δ::hph lys1⁺::GFP-bqt4(Δ384-413aa)*	This study	S3
H1N2796	*h⁻ lys1⁺::nmt1p-GFP aur1ʳ::adh1p-mRFP-GST-NLS*	This study	S5
H1N2797	*h⁻ lys1⁺::nmt1p-GFP-bqt4 aur1ʳ::adh1p- mRFP-GST-NLS*	This study	S5
H1N2798	*h⁻ lys1⁺::nmt1p-GFP-bqt4-KSE(364-383 aa) aur1ʳ::adh1p- mRFP-GST-NLS*	This study	S5
H1N2799	*h⁻ lys1⁺::nmt1p-GFP-bqt4-IDR(364-413 aa) aur1ʳ::adh1p- mRFP-GST-NLS*	This study	S5
H1N2800	*h⁻ lys1⁺::nmt1p-GFP-bqt4-IDRTM(364-432 aa) aur1ʳ::adh1p- mRFP-GST-NLS*	This study	S5
YK893	*h⁻ ura4-D/SE ade6-210 imr1L::ura4⁺ otr1R::ade6⁺ aur1ʳ::pYC19*	Kinugasa et al (2019)	S6a
H1N2738	*h⁻ ura4-D/SE ade6-210 imr1L::ura4⁺ otr1R::ade6⁺ aur1ʳ::nmt1p-GFP-bqt4*	This study	S6a
H1N2741	*h⁻ ura4-D/SE ade6-210 imr1L::ura4⁺ otr1R::ade6⁺ aur1ʳ::nmt1p-GFP-bqt4-IDRTM(364-432a.a.)*	This study	S6a
YK896	*h⁻ ura4-D/SE ade6-210 imr1L::ura4⁺ otr1R::ade6⁺ clr4Δ::kanʳ aur1ʳ::pYC19*	Kinugasa et al (2019)	S6a
H1N2668	*h⁻ bqt4Δ::hph lem2⁺-mcherry::kanʳ lys1⁺::nmt1p-GFP*	This study	S6b
H1N2669	*h⁻ bqt4Δ::hph lem2⁺-mcherry::kanʳ lys1⁺::nmt1p-GFP-bqt4*	This study	S6b
H1N2670	*h⁻ bqt4Δ::hph lem2⁺-mcherry::kanʳ lys1⁺::nmt1p-GFP-bqt4-KSE(364-383aa)*	This study	S6b
H1N2671	*h⁻ bqt4Δ::hph lem2⁺-mcherry::kanʳ lys1⁺::nmt1p-GFP-bqt4-IDR(364-413aa)*	This study	S6b
H1N2747	*h⁻ lys1⁺::nmt1p-GFP-bqt4 lem2Δ::kanʳ cnp1⁺-FL5-mCherry::hph*	This study	S6c
H1N2748	*h⁻ lys1⁺::nmt1p-GFP-bqt4-KSE(364-383aa) lem2Δ::kanʳ cnp1⁺-FL5-mCherry::hph*	This study	S6c
H1N2749	*h⁻ lys1⁺::nmt1p-GFP-bqt4-IDR(364-413aa) lem2Δ::kanʳ cnp1⁺-FL5-mCherry::hph*	This study	S6c
H1N2750	*h⁻ lys1⁺::nmt1p-GFP-bqt4-IDRTM(364-432aa) lem2Δ::kanʳ cnp1⁺-FL5-mCherry::hph*	This study	S6c
H1N1865	*h⁻ bqt4Δ::hph Ish1⁺-mCherry::bsd lys1⁺::bqt4p-GFP-bqt4*	This study	S7a
H1N2801	*h⁻ lys1⁺::nmt1p-GFP-bqt4-IDRTM(364-432 aa) aur1ʳ::nda3p-atb2-mCherry*	This study	M2

S. cerevisiae strains

Strain	Genotype	Source	Figure
AH109	*MATa*, *trp1-901*, *leu2-3*, *112*, *ura3-52*, *his3-200*, *gal4Δ*, *gal80Δ*, *LYS2*::$GAL1_{UAS}$-$GAL1_{TATA}$-*HIS3*, *MEL1*, $GAL2_{UAS}$-$GAL2_{TATA}$-*ADE2*, *URA3*::$MEL1_{UAS}$-$MEL1_{TATA}$-*lacZ*)	Clontech, Takara Bio	

H1N2190	AH109 harboring pGADT7 and pGBKT7	Le et al (2023)	S1b
H1N2191	AH109 harboring pGADT7-bqt4 and pGBKT7	This study	S1b
H1N2192	AH109 harboring pGADT7-bqt4(Δ364-383aa.) and pGBKT7	This study	S1b
H1N2193	AH109 harboring pGADT7 and pGBKT7-bqt3	Le et al (2023)	S1b
H1N2194	AH109 harboring pGADT7-bqt4 and pGBKT7-bqt3	This study	S1b
H1N2195	AH109 harboring pGADT7-bqt4(Δ364-383aa.) and pGBKT7-bqt3	This study	S1b

Legends to Supplementary Movie

Supplementary Movie 1 Detachment and declustering of centromeres from the NE by Bqt4 overexpression

GFP-tagged IDR-TM (green) was expressed under the control of the *nmt1* promoter in cells expressing Cnp1-mCherry (magenta) as a centromere marker. The cells were pre-cultured in EMMG+1 μM YAM2 for overnight, washed, and then observed using fluorescence microscopy. The bright-field image is shown on the right. The elapsed time is denoted as h:min:s. The scale bar indicates 10 μm.

Supplementary Movie 2 Chromosome segregation defect by Bqt4 overexpression

GFP-tagged IDR-TM (green) was expressed under control of the *nmt1* promoter in cells expressing Atb2-mCherry (magenta). The cells were pre-cultured in EMMG+1 μM YAM2 overnight, washed, and then observed using fluorescence microscopy. The elapsed time is denoted as h:min:s. Scale bar: 5 μm.